

---

# Understanding and Exploiting Weight Update Sparsity for Communication-Efficient Distributed RL

---



Erfan Miah<sup>\*</sup>  
Covenant AI

Eugene Belilovsky  
Mila, Concordia University

## Abstract

Reinforcement learning (RL) is a critical component for post-training large language models (LLMs). However, in bandwidth-constrained distributed RL, scalability is often bottlenecked by the synchronization of policy weights from trainers to inference workers, particularly over commodity networks or in decentralized settings. While recent studies suggest that RL updates modify only a small fraction of model parameters, these observations are typically based on coarse checkpoint differences. We present a systematic empirical study of weight-update sparsity at both step-level and multi-step granularities, examining its evolution across training dynamics, off-policy delay, and model scale. We find that update sparsity is consistently high, frequently exceeding 99% across practically relevant settings. Leveraging this structure, we propose PULSE (Patch Updates via Lossless Sparse Encoding), a simple yet highly efficient **lossless** weight synchronization method that transmits only the indices and values of modified parameters. PULSE is robust to transmission errors and avoids floating-point drift inherent in additive delta schemes. In bandwidth-constrained decentralized environments, our approach achieves over **100**× (14 GB → ~108 MB) communication reduction while maintaining bit-identical training dynamics and performance compared to full weight synchronization. By exploiting this structure, PULSE enables decentralized RL training to approach centralized throughput, reducing the bandwidth required for weight synchronization from 20 Gbit/s to 0.2 Gbit/s to maintain high GPU utilization.

## 1 Introduction

Reinforcement learning (RL) is widely used for post-training large language models (LLMs). Reinforcement Learning from Human Feedback (RLHF) [1–3] uses human preference data to encourage instruction-following behavior. Reinforcement Learning from AI Feedback (RLAIF) [4, 5] scales this approach by substituting human annotators with AI models. Reinforcement Learning with Verifiable Rewards (RLVR) uses tasks with programmatically verifiable outcomes, such as mathematics and code, to provide objective reward signals [6, 7]. Together, these approaches are now a common stage in LLM training pipelines, alongside pre-training and supervised fine-tuning [7–11].

Modern RL pipelines typically decouple training from inference: specialized inference engines generate rollouts up to 12× faster than general-purpose training frameworks [12–14]. But this architecture requires frequent and communication heavy weight synchronization [12, 13]. For a 7B model in 16-bit precision, each synchronization transfers 14 GB to each inference worker. As

---

<sup>\*</sup>Correspondence to: [erfan@covenant.ai](mailto:erfan@covenant.ai)

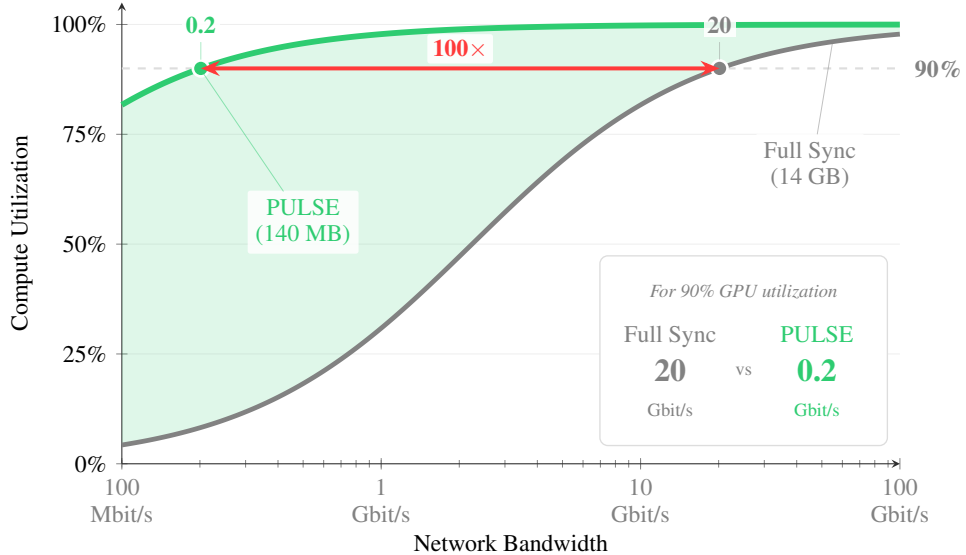


Figure 1: **Compute utilization vs. network bandwidth** for a 7B model with 50s/step compute time. Full weight synchronization (14 GB) requires 20 Gbit/s links for 90% GPU utilization. PULSE reduces this to 0.2 Gbit/s (a **100 $\times$**  reduction) by transmitting only the 1% of parameters that change (140 MB). This enables efficient training over standard network connections, where the global median fixed broadband speed is low. We validate this in a live decentralized network in Section 5.

Figure 1 illustrates, maintaining 90% GPU utilization requires 20 Gbit/s links, far exceeding typical commodity bandwidth. The problem is acute in geo-distributed settings; for example, Prime Intellect Team et al. [15] reports that broadcasting a 32B checkpoint takes approximately 14 minutes over the public internet.

While the communication bottleneck in distributed training has traditionally motivated extensive research into gradient compression [16–18], these methods are often ill-suited for the weight-synchronization demands of modern RL pipelines. Most gradient-based approaches are lossy, introducing approximation errors that require mitigation through techniques such as error feedback [19] or extensive hyperparameter tuning. Furthermore, they focus on the *aggregation* of updates between trainers rather than the *broadcast* of new parameters to inference workers. In contrast, lossless techniques such as entropy coding [20] have historically yielded only modest gains with compute overhead, failing to bridge the bandwidth gap required for geo-distributed training.

Separately, Mukherjee et al. [21] observe that RL fine-tuning updates only a small “subnetwork” of 5–30% of parameters, attributing this to training on in-distribution data. However, their analysis measures accumulated changes between initial and final checkpoints using an approximate threshold ( $10^{-5}$ ), without examining the mechanism at per-step granularity. We provide a complementary perspective. Analyzing **bitwise** per-step sparsity, we find that the phenomenon arises from the interaction between BF16 precision and learning rate: gradients remain nearly fully dense ( $\sim 99\%$  non-zero), but BF16’s limited mantissa means updates must exceed a weight-dependent threshold to take effect. At standard RL learning rates ( $\sim 3 \times 10^{-6}$ ), most updates fall below this threshold and are absorbed. This mechanistic understanding is essential for practitioners who wish to preserve sparsity, and it enables the **lossless** compression we propose for distributed RL training.

To exploit this sparsity for communication-efficient synchronization, we must first establish that it is reliable in practice. Sparsity must be *consistently high* throughout training, not just at convergence. It must be *mechanistically understood*, so practitioners know which configurations preserve it. And it must be *robust* to practical deployment scenarios, including asynchronous updates where inference nodes operate on stale weights. These requirements motivate our empirical investigation across training progression, model scales (0.5B to 7B), and off-policy conditions, culminating in a **provably lossless** synchronization method.

We make three contributions:

1. We provide a mechanistic analysis showing that weight-update sparsity arises primarily from the interaction between BF16 precision and RL’s conservative learning rates. We validate that sparsity is consistently high ( $\sim 99\%$ ), mechanistically predictable, and robust to off-policy delay, enabling over  $100\times$  compression (Section 3).
2. We introduce PULSE (Patch Updates via Lossless Sparse Encoding), a **lossless** synchronization method that transmits only changed parameter indices and their new values. By storing actual values rather than additive deltas, we avoid floating-point drift in multi-hop reconstruction. We provide bandwidth-aware guidance for compression algorithm selection (Section 4).
3. We demonstrate PULSE on a live decentralized network where nodes communicate over the public internet, achieving **over 100 $\times$**  bandwidth reduction (from 20 Gbit/s to 0.2 Gbit/s for 90% GPU utilization) while training successfully on mathematical reasoning tasks (Section 5).

The remainder of this paper is organized as follows. Section 2 provides background on GRPO and off-policy considerations in distributed training. Section 3 presents our empirical study of weight update sparsity and its compression potential. Section 4 details the PULSE method and practical compression choices. Section 5 validates our approach on a decentralized training network. Section 6 discusses limitations and future directions.

## 2 Background and Problem Formulation

This section establishes the technical foundations for our approach: the GRPO algorithm used throughout our experiments and the formalization of off-policy delay in distributed training.

### 2.1 RL for Reasoning with GRPO

We focus on reinforcement learning for reasoning tasks with *verifiable rewards* (RLVR) [7], where rewards are computed by an automatic verifier (e.g., final-answer matching, unit tests) rather than learned human preferences.<sup>2</sup>

**Setup.** Let  $\pi_\theta$  denote a language model policy parameterized by  $\theta$ . Given a prompt  $x$ , the policy generates a response  $y \sim \pi_\theta(\cdot|x)$ . A verifier defines a reward function  $r(x, y) \in \{0, 1\}$  indicating whether  $y$  satisfies the task constraints (e.g., correct final answer).

**GRPO.** We use Group Relative Policy Optimization (GRPO) [6], the dominant algorithm for training reasoning models [7, 22]. GRPO estimates advantages from group-relative rewards without requiring a learned value function. For each prompt  $x$ , GRPO samples a group of  $G$  responses  $\{y_i\}_{i=1}^G$  and computes advantages relative to the group mean:

$$\hat{A}_i = \frac{r(x, y_i) - \bar{r}}{\sigma_r}, \quad \text{where } \bar{r} = \frac{1}{G} \sum_{j=1}^G r(x, y_j) \quad (1)$$

The policy is updated using a clipped surrogate objective similar to PPO [23]. Following recent work [22, 24], we omit the KL divergence penalty; Mukherjee et al. [21] showed this does not substantially affect sparsity. We provide the full mathematical formulation in Section E.1.

### 2.2 Off-Policy Considerations in Distributed Training

In distributed RL training, different inference workers may operate with different versions of the model weights. We formalize this through the concept of off-policy delay.

**Definition 2.1** (Off-Policy Delay). Let  $\theta_t$  denote the current model parameters at optimization step  $t$ . A rollout generated using parameters  $\theta_{t-k}$  is said to have an **off-policy delay** of  $k$  steps.

In practice, this delay arises from asynchronous updates, communication latency, and batching. This off-policy delay has implications for both training dynamics and, as we will show, for the sparsity structure of weight updates.

---

<sup>2</sup>While our experiments focus on GRPO for reasoning tasks, prior work observed similar sparsity patterns for PPO-based RLHF [21], suggesting this is a general phenomenon in RL post-training. We plan to extend our analysis to other algorithms (e.g., PPO, DPO) in future versions.

### 3 Characterizing Weight Update Sparsity

For sparse weight updates to enable communication-efficient synchronization, three conditions must hold: sparsity must be *consistently high* throughout training, *mechanistically understood* so practitioners can preserve it, and *robust* to practical deployment scenarios. This section establishes all three and quantifies the resulting compression potential, directly informing the design of PULSE (Section 4).

#### 3.1 Experimental Setup

**Models.** We conduct experiments on three model families: Qwen2.5-Instruct [25] at 0.5B, 1.5B, and 7B parameters; Llama-3.2-Instruct [26] at 3B parameters; and Gemma-3-4B-it [27].

**Training algorithm.** We use GRPO (Section 2.1) with hyperparameters based on DAPO [22]: learning rate  $3 \times 10^{-6}$ , clipping  $\epsilon_{\text{low}} = 0.2$ ,  $\epsilon_{\text{high}} = 0.28$ , 32 prompts per batch with 16 rollouts each. We report results averaged over 4 random seeds.

**Dataset.** We train on mathematical reasoning tasks using reinforcement learning with verifiable rewards (RLVR) [7]. Specifically, we use the MATH dataset [28]. From the 7,500 training examples (spanning multiple subjects), we extract a stratified 500-example validation split that remains fixed throughout training; the remaining 7,000 problems form our training set. We sample rollouts with temperature 1.0 and top- $p = 1.0$  to encourage exploration, following DeepSeek-AI et al. [7].

Additionally, we demonstrate in Section 5 that these findings generalize beyond mathematical reasoning to code generation tasks.

**Reward.** We use reinforcement learning with verifiable rewards (RLVR) [7]. For mathematical reasoning, we use a composite reward based on correctness, formatting, and thinking presence. Full reward formulations for both tasks are provided in Section C.3.

**Training duration.** We train for 400 steps. This duration is sufficient to observe both early-training dynamics and stable-phase behavior while remaining computationally tractable across multiple model scales and experimental conditions. We verify that training has converged within this window by examining pass@1 accuracy curves on validation sets across all models (Section D.2); performance plateaus by step 400 in most cases.

**Sparsity metric.** We measure *weight update sparsity* as the fraction of parameters that remain bitwise identical between consecutive optimization steps. Formally, given parameters  $\theta_t$  at step  $t$ , sparsity is  $|\{i : \theta_{t+1}^{(i)} = \theta_t^{(i)}\}|/d$  where  $d$  is the total parameter count. Higher sparsity indicates fewer changed parameters and greater potential for compression. We provide formal definitions, including the generalization to  $k$ -step sparsity (comparing  $\theta_t$  to  $\theta_{t+k}$ ), in Section A.1.

#### 3.2 How Sparse Are Updates Throughout Training?

Figure 2 summarizes our findings across all models. Mean per-step weight update sparsity is approximately 99% across all model scales, confirming and extending prior observations by Mukherjee et al. [21] to the GRPO setting and instruction-tuned models. This consistently high sparsity indicates that the vast majority of parameters remain unchanged at each optimization step, a structure we exploit for communication efficiency in Section 4.

**Scale and architecture.** Sparsity is remarkably consistent across model families (Qwen, Llama, Gemma) and scales (0.5B–7B), with all models achieving 98.9%–99.4% per-step sparsity despite architectural differences. This consistency suggests the phenomenon is fundamental to Adam optimization with RL fine-tuning rather than model-specific.

**Stability throughout training.** Sparsity remains remarkably stable across the entire training trajectory: standard deviation across 400 steps is only 0.2–0.4%. This low variability indicates that sparsity is not a transient early-training phenomenon but a persistent property. Critically, even the

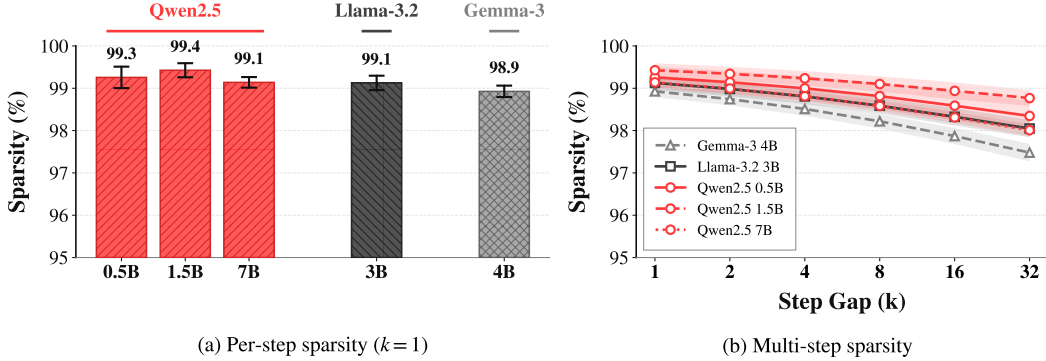


Figure 2: **Weight update sparsity across model scales and families.** (a) Mean per-step sparsity (%) averaged over 400 training steps. Error bars indicate  $\pm 1$  standard deviation across steps. (b) Sparsity when comparing  $\theta_t$  to  $\theta_{t+k}$  for increasing  $k$ . Shaded regions indicate  $\pm 1$  standard deviation. Within the recommended  $k \leq 8$  range for asynchronous RL [29], sparsity remains above 98% for all models.

*minimum* sparsity (worst-case step) remains above 98% for all models, providing reliable guarantees for method design.

**Multi-step sparsity.** When measuring sparsity over multiple steps (i.e., comparing  $\theta_t$  to  $\theta_{t+k}$  for  $k > 1$ ), sparsity remains high but decreases slightly as more parameters accumulate changes (Figure 2). Recent work identifies  $k = 8$  as optimal for asynchronous RL, demonstrating that off-policy delays up to this level do not materially affect asymptotic performance while substantially improving compute efficiency [29]. Within this recommended range ( $k \leq 8$ ), sparsity remains above 98% for all models. Sparsity degrades gracefully beyond this range, with all models maintaining above 97% at  $k = 32$ .

### Takeaway 1: Baseline Sparsity

RL fine-tuning produces highly sparse weight updates ( $\sim 99\%$  per-step) across model scales and families. Within the recommended  $k \leq 8$  operating range for asynchronous RL, sparsity remains above 98% for all models tested, providing reliable guarantees for communication-efficient method design.

## 3.3 Understanding and Preserving Sparsity

Having established that sparsity is consistently high, we now investigate its underlying mechanism and robustness. Understanding why sparsity occurs allows practitioners to preserve it; understanding what affects it ensures robustness in practical deployments.

### 3.3.1 Why Are Gradients Dense but Updates Sparse?

A natural hypothesis is that weight update sparsity arises from sparse gradients. However, our measurements reveal the opposite: **gradients are nearly fully dense**, with approximately 99% of parameters receiving non-zero gradients at each step (Section D.1). The sparsity emerges downstream, during the weight update itself, through a phenomenon we call *update absorption*: modern LLM training uses BF16 precision, which has limited resolution, so updates smaller than roughly  $|w|/256$  of a weight’s magnitude cannot be represented and are rounded away. Since the learning rate directly scales update magnitudes, it determines which weights can be modified. At standard RL learning rates ( $\eta \approx 3 \times 10^{-6}$ ), most updates fall below this threshold and are absorbed. We provide formal definitions and analysis in Section A.2. This analysis assumes Adam-style optimizers; other optimizers may exhibit different behavior (Section A.6).

Figure 3 visualizes the interaction between learning rate, weight magnitudes, and BF16 precision. The diagonal line shows the minimum update magnitude required to modify a weight of a given size. Adam updates have two relevant bounds: the *effective bound* where update magnitude equals

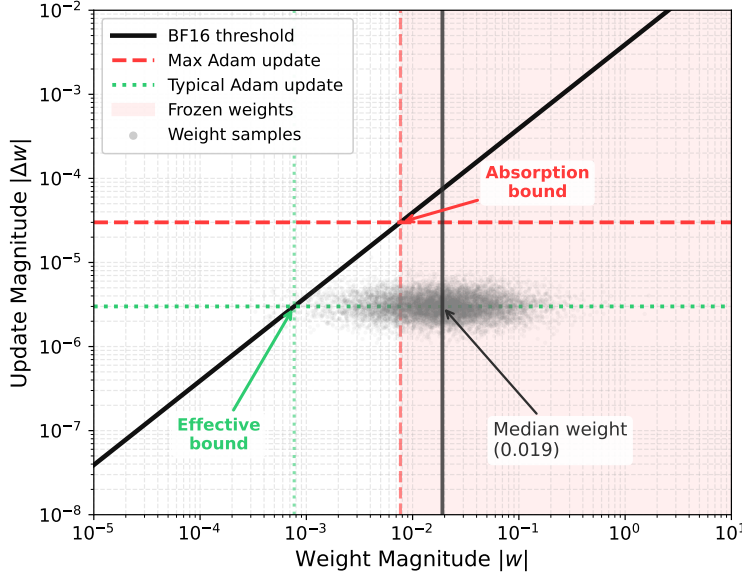


Figure 3: **Why most weights cannot be updated in BF16.** The diagonal line shows the minimum update size needed to change a weight (larger weights require larger updates). Horizontal lines show Adam update bounds at learning rate  $3 \times 10^{-6}$ : the effective bound ( $\eta$ ) and the absorption bound ( $10\eta$ ). The shaded region marks weights beyond the absorption bound, which are permanently frozen. Gray dots show that most LLM weights fall in this region, explaining the observed sparsity.

the learning rate  $\eta$  (the practical case when Adam’s ratio  $|\hat{m}|/\sqrt{\hat{v}} \approx 1$ ), and the *absorption bound* representing the theoretical maximum update ( $10\eta$  for standard hyperparameters). Where these horizontal lines intersect the diagonal marks the corresponding weight thresholds. Weights beyond the absorption bound are permanently frozen; weights between the two thresholds may occasionally receive updates under extreme gradient conditions but are typically frozen.

The key observation is that most LLM weights (gray dots) lie far to the right of where the update bound intersects the threshold line. For these weights, even maximal gradients cannot produce updates large enough to survive BF16 rounding. This explains why approximately 96% of weights cannot receive updates based on magnitude alone (see Section A.4 for detailed statistics across model families).

Learning rate is the primary factor controlling sparsity. Since update magnitude scales linearly with learning rate, raising the learning rate shifts the horizontal lines upward in Figure 3, allowing more weights to receive updates. This predicts that higher learning rates should reduce sparsity. Figure 4a confirms this prediction: as learning rate increases from  $5 \times 10^{-7}$  to  $5 \times 10^{-6}$ , sparsity decreases monotonically for all values of  $k$ . The effect is more pronounced at higher  $k$ , but even at  $k = 32$  and the highest learning rate tested, sparsity remains above 97%.

These findings reveal that the high sparsity of RL fine-tuning is not incidental but *inherent* to practical training configurations. Prior work [21, 30, 31] observed this sparsity and attributed it variously to RL optimization dynamics or BF16 precision. Our analysis unifies these perspectives: BF16 creates the absorption mechanism, and the small learning rates required for stable RL training amplify its effect. This is independently confirmed by Shenfeld et al. [30], who showed that training with pure FP32 eliminates sparsity entirely while achieving identical model performance. Importantly, this refers to pure FP32 training; mixed-precision training, where BF16 is used for computation while optimizer master weights remain in FP32 [13, 32], preserves the same level of sparsity (Section A.2). Practitioners using standard training pipelines benefit from this sparsity without additional effort. Moreover, this mechanism predicts that lower-precision formats (e.g., FP8) will exhibit even higher sparsity, compounding computational savings with reduced communication costs.

### Takeaway 2: Learning Rate Controls Sparsity

Sparsity arises primarily from the interaction between BF16 precision and learning rate. At standard RL learning rates, most updates are absorbed. Higher learning rates reduce sparsity but destabilize RL training. *High sparsity is inherent to practical RL fine-tuning configurations.*

#### 3.3.2 How Does Policy Staleness Affect Sparsity?

In distributed RL, rollouts are often generated using stale policy weights while the learner performs gradient updates. This *policy staleness* is common in asynchronous training. We investigate how it affects sparsity. Concretely, a staleness of  $N$  means rollouts are regenerated every  $N$  gradient steps:  $N = 1$  is fully on-policy, while  $N > 1$  corresponds to one on-policy update followed by  $N - 1$  off-policy updates using the same rollouts.

Figure 4b shows how both policy staleness and measurement granularity affect sparsity. For per-step updates ( $k = 1$ ), sparsity remains above 98.5% even at 32-step staleness. When measuring over longer intervals (higher  $k$ ), sparsity decreases as more parameters accumulate changes, but remains above 97.5% across all conditions tested. The shaded error bands show that variance increases modestly with both staleness and  $k$ , but the degradation is graceful and predictable.

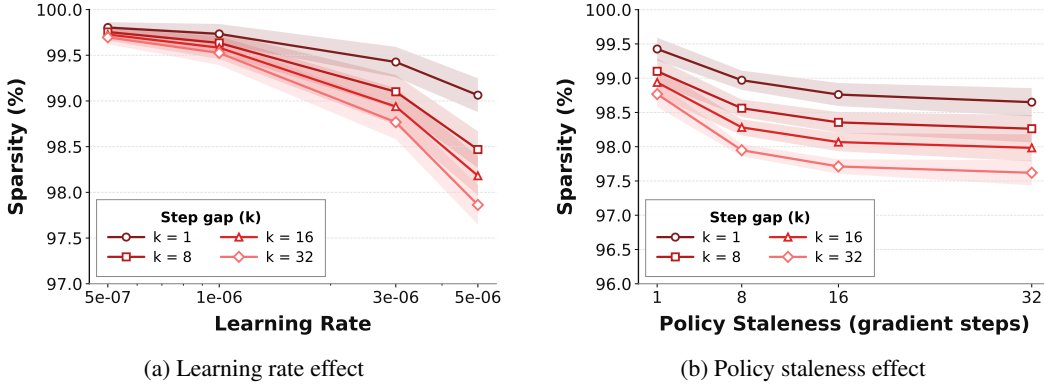


Figure 4: **Factors affecting weight update sparsity.** (a) Impact of learning rate: each line shows  $k$ -step sparsity as a function of learning rate. Higher learning rates reduce sparsity by increasing update magnitudes above the BF16 absorption threshold. (b) Impact of policy staleness:  $k$ -step sparsity as a function of gradient steps between weight synchronizations. Higher staleness modestly degrades sparsity but the effect is small. Shaded regions indicate  $\pm 1$  standard deviation across training steps.

### Takeaway 3: Policy Staleness

Sparsity is robust to policy staleness: even 32-step staleness reduces per-step sparsity by less than 1 percentage point (from  $\sim 99.4\%$  to  $\sim 98.7\%$ ). *Asynchronous distributed training with delayed synchronization remains compatible with sparse communication.*

#### 3.4 Communication Implications

Having established that weight update sparsity is high, mechanistically understood, and robust, we now quantify its implications for communication efficiency.

**Compression potential.** At 99% sparsity, only 1% of parameters change between steps. A sparse representation that stores indices and values of changed parameters, combined with delta encoding and general-purpose compression (e.g., zstd), achieves  $56\text{--}100\times$  total bandwidth reduction depending on algorithm and model (Section E.4). The lower bound ( $56\times$ ) corresponds to fast algorithms like

lz4; our default configuration using zstd-1 achieves  $79\times$  on average, with some architectures reaching  $100\times$ .

**Bandwidth implications.** This compression transforms the bandwidth requirements for weight synchronization. For a 7B model, training steps typically take 30–90 seconds depending on context length and hardware [12]. At 60 seconds per step, full checkpoint synchronization requires  $14\text{ GB}/60\text{ s} \approx 1.9\text{ Gbit/s}$  sustained throughput. With sparse synchronization at  $79\times$  compression (our default configuration), this drops to  $\sim 24\text{ Mbit/s}$ , well within commodity internet capacity. The next section presents PULSE, which realizes this compression while guaranteeing lossless reconstruction, and provides practical guidance for compression algorithm selection based on available bandwidth.

#### Takeaway 4: Communication Efficiency

The  $\sim 99\%$  sparsity observed in RL fine-tuning enables  $56\text{--}100\times$  communication reduction (typically  $79\times$  with zstd-1), transforming weight synchronization from a high-bandwidth bottleneck to a commodity-network-compatible operation.

## 4 The PULSE Method

Building on the sparsity characterization and compression potential established in Section 3, we present PULSE (Patch Updates via Lossless Sparse Encoding), a lossless synchronization method that realizes the theoretical bandwidth reduction while guaranteeing bit-exact reconstruction. This section describes the core algorithm (Section 4.1), the distributed system architecture (Section 4.2), and practical compression choices (Section 4.3).

### 4.1 Sparse Value Patching

The core idea of PULSE is to transmit only parameters that have changed between training steps, then *patch* the model at the receiving end. A **patch**  $P = (\mathcal{I}, \mathcal{V})$  consists of indices  $\mathcal{I}$  of changed parameters and their new values  $\mathcal{V}$ , compressed for transmission (Algorithm 1).

---

#### Algorithm 1 Sparse Value Patching

---

```

1: procedure ENCODE( $W_t, W_{t-1}$ )
2:    $\mathcal{I} \leftarrow \{i : W_t^{(i)} \neq W_{t-1}^{(i)}\}$                                 // Bitwise comparison
3:    $\mathcal{V} \leftarrow W_t[\mathcal{I}]$                                          // Extract new values (not deltas)
4:    $\mathcal{I} \leftarrow \text{SORT}(\mathcal{I})$ ;  $\mathcal{I} \leftarrow \text{DELTAEENCODE}(\mathcal{I})$           // Optional: delta encoding
5:    $\mathcal{I} \leftarrow \text{DOWNCAST}(\mathcal{I})$                                          // Optional: narrow integer types
6:    $P \leftarrow \text{COMPRESS}(\mathcal{I}, \mathcal{V})$                                          // e.g., zstd
7:   return  $P$ 
8: end procedure

9: procedure DECODE( $W_{t-1}, P$ )
10:   $(\mathcal{I}, \mathcal{V}) \leftarrow \text{DECOMPRESS}(P)$ 
11:   $\mathcal{I} \leftarrow \text{UPCAST}(\mathcal{I})$                                          // Restore original integer type
12:   $\mathcal{I} \leftarrow \text{DELTADECODE}(\mathcal{I})$                                          // Recover absolute indices
13:   $W_t \leftarrow W_{t-1}$ ;  $W_t[\mathcal{I}] \leftarrow \mathcal{V}$                                          // Patch
14:  return  $W_t$ 
15: end procedure

```

---

**Encoding.** Given consecutive checkpoints  $W_{t-1}$  and  $W_t$ , we identify differing positions via bitwise comparison in a single  $O(d)$  pass. For each changed position, we store its index and **new value** (not the arithmetic difference). This design choice is critical: storing actual values avoids floating-point drift that would accumulate with additive delta schemes.

To maximize compression, we apply two optional optimizations before general-purpose compression: (1) **delta encoding** sorts indices and stores differences between consecutive indices rather than absolute positions, exploiting spatial locality; (2) **type downscaling** represents these small deltas

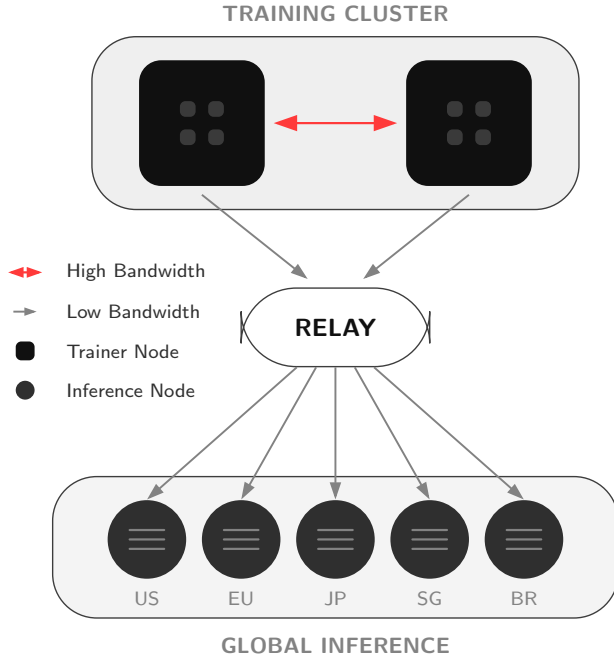


Figure 5: **PULSE synchronization topology.** Training nodes use high-bandwidth interconnects for dense gradient communication. Sparse weight patches are published to a central relay, enabling inference nodes to synchronize over commodity networks.

using narrower integer types (e.g., `uint16` instead of `int32`). Together, these contribute  $\sim 23\%$  additional compression beyond the sparse representation alone (Section E.4).

**Decoding.** Reconstruction reverses this pipeline: decompress, recover absolute indices from deltas, then overwrite positions  $W_t[\mathcal{I}] \leftarrow \mathcal{V}$ . This is a direct memory copy with no floating-point arithmetic, guaranteeing bit-identical reconstruction regardless of how many patches are chained.

## 4.2 Distributed Synchronization

The sparsity we exploit exists in weight updates, not gradients. As established in Section 3.3.1, gradients remain nearly fully dense ( $\sim 99\%$  non-zero) and require lossy compression [16, 17], while weight updates exhibit high sparsity ( $\sim 1\%$  changed) that enables lossless compression. This asymmetry motivates a natural system topology (Figure 5): training nodes stay colocated with high-bandwidth interconnects for dense gradient communication, while inference nodes can synchronize over commodity networks using sparse patches. Inference dominates compute in RL post-training at a 4:1 FLOP ratio [15], so the number of inference nodes typically exceeds the number of training nodes. Crucially, weight synchronization is a *broadcast* operation from training nodes to these many inference nodes, unlike gradient aggregation which uses bandwidth-efficient allreduce collectives. This fan-out pattern makes weight transfer particularly sensitive to bandwidth constraints, as the same payload must reach every inference worker.

Training nodes publish sparse patches to centralized object storage (e.g., Cloudflare R2, AWS S3), while inference nodes pull updates independently. This decoupled architecture allows training and inference to scale independently. As shown in Section 3.3.2, sparsity remains robust under policy staleness up to 32 steps, making asynchronous operation practical.

**Checkpoint chain structure.** To balance efficiency with robustness, PULSE organizes updates into a chain of sparse patches anchored by periodic full checkpoints (Figure 14).

Training nodes publish a full checkpoint every  $k$  steps (the *anchor interval*). Between anchors, they publish only sparse patches. Each patch includes a SHA256 hash of the resulting weights for integrity verification.

Inference nodes synchronize via two paths depending on their state. In the *fast path*, a node already synchronized to step  $t - 1$  downloads and applies a single patch to reach step  $t$ . Conversely, the *slow path* handles nodes that join late or miss steps: they download the nearest anchor checkpoint and apply up to  $k - 1$  subsequent patches. Recovery latency scales with the anchor interval  $k$ , where smaller  $k$  reduces worst-case recovery time at the expense of increased storage overhead from more frequent full checkpoints.

Further details on the synchronization mechanism, including anchor interval selection, integrity verification, and failure recovery, are provided in Section G.

### 4.3 Compression Algorithm Selection

The optimal compression algorithm depends on available bandwidth. At high bandwidth, encoding time dominates, so fast algorithms (lz4) minimize total transfer time. At low bandwidth, network time dominates, so higher-ratio algorithms (zstd-3) are preferable. For a 7B model at 99% sparsity, we identify three primary regimes:

- **Datacenter** ( $>800$  Mbit/s): lz4 (56 $\times$  compression, 830 MB/s encode)
- **Typical cloud** (14–800 Mbit/s): zstd-1 (79 $\times$ , 530 MB/s) [*default*]
- **Constrained** ( $<14$  Mbit/s): zstd-3 (80 $\times$ , 197 MB/s)

Figure 13 in the appendix visualizes these bandwidth tiers and the resulting algorithm selection. See Section E.4 for detailed ablations, per-model breakdowns, and the selection methodology.

**Implementation.** PULSE is integrated into grail, our open-source framework for decentralized RL post-training.<sup>3</sup> The default configuration uses 2D COO representation with delta encoding, type downscaling, and zstd-1 compression, which provides the best throughput-compression tradeoff for commodity networks (Section E.4). Full implementation details are in Section E.

## 5 PULSE in Practice

We validate PULSE on grail [33], a decentralized reinforcement learning platform where geographically distributed nodes communicate over the public internet with heterogeneous bandwidth. grail employs a fully asynchronous architecture: the trainer runs continuously, sampling from a replay buffer while background processes handle checkpoint uploads and rollout downloads at window boundaries. Validators ensure rollouts originate from the correct checkpoint via hidden-state fingerprinting. See Section B for architectural details.

**Setup.** To demonstrate the domain-agnostic nature of PULSE, we evaluate on two distinct RLVR tasks: (1) mathematical reasoning using the MATH dataset with Qwen2.5-7B-Instruct (identical to the setup in Section 3), and (2) code generation using the MBPP dataset [34] with Qwen2.5-Coder-7B-Instruct. For MBPP, we use 774 tasks for training and 190 for validation, with rewards based on test pass rates and syntax validity (see Section C.3). For each task, we conduct 3 independent trials. Hyperparameters follow Section 3.1, except we use a lower learning rate ( $1 \times 10^{-6}$ ) for training stability in the decentralized setting. Full details are in Section C.2.

**Bandwidth reduction.** Figure 6 demonstrates that the high sparsity observed in Section 3 translates directly to communication savings in practice. Upload sizes average 108 MB (SE: 1.1 MB), more than 100 $\times$  smaller than the 14 GB required for full 7B model synchronization. At the mean, PULSE achieves approximately 130 $\times$  bandwidth reduction, exceeding the 79 $\times$  observed at the benchmark learning rate ( $3 \times 10^{-6}$ ) in Section 3.4. This improvement is consistent with the higher sparsity induced by the lower learning rate ( $1 \times 10^{-6}$ ), as predicted by our analysis in Section 3.3.1.

<sup>3</sup><https://github.com/one-covenant/grail>

**Training effectiveness.** Despite transmitting only sparse updates, training proceeds normally. Validation pass@1 improves steadily throughout training, reaching final improvements of +50.1 and +49.4 percentage points on MATH and MBPP respectively. Standard deviation across runs remains low ( $\leq 1.5$  percentage points).

**Lossless reconstruction.** All weight transfers pass SHA-256 verification, confirming bitwise-identical reconstruction at inference nodes. This validates the core premise of PULSE: the sparsity induced by BF16 precision enables *lossless* compression without approximation error or error feedback mechanisms.

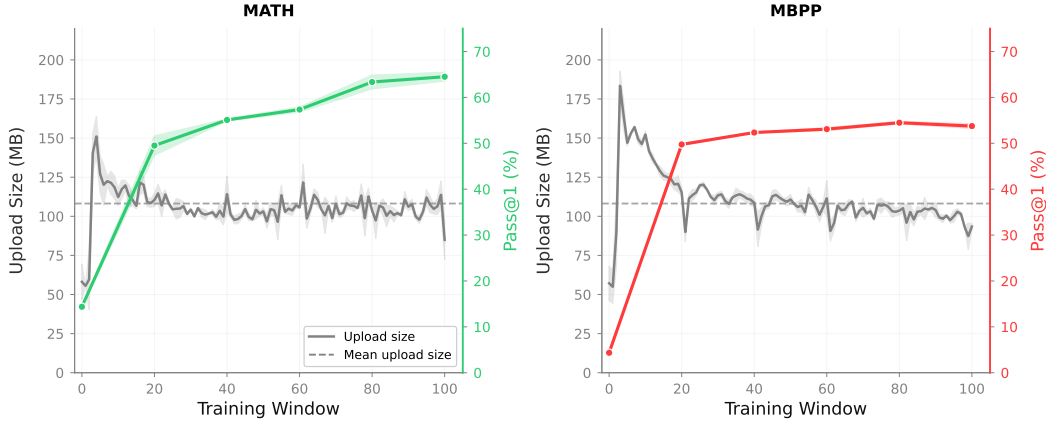


Figure 6: **Training progress with PULSE.** Validation pass@1 (colored lines) improves steadily while upload sizes (gray lines) remain stable throughout training. Each training window corresponds to approximately 6 minutes, during which up to 8 gradient steps may occur; the exact count varies due to the asynchronous nature of the system. The dashed line indicates the mean upload size of 108 MB, representing more than 100 $\times$  reduction compared to the 14 GB required for full checkpoint synchronization. Shaded regions indicate  $\pm 1$  standard error across 3 independent runs.

## 6 Conclusion

We have shown that weight updates in RL fine-tuning exhibit remarkable sparsity: approximately 99% of parameters remain unchanged at each optimization step, a phenomenon arising from the interaction between BF16 precision and the conservative learning rates typical of RL. This sparsity is consistent across model scales (0.5B–7B), training stages, and off-policy delays up to 32 steps.

Building on this observation, we introduced PULSE, a lossless checkpoint synchronization method that exploits update sparsity by transmitting only the parameters that actually change. Unlike delta-based approaches that accumulate quantization error over time, PULSE stores actual weight values, providing mathematical guarantees of bitwise-identical reconstruction. In practice, this achieves over 100 $\times$  bandwidth reduction compared to full checkpoint synchronization.

We validated PULSE on a decentralized RL training network, where it maintained identical training dynamics to full synchronization while reducing communication costs by two orders of magnitude. This demonstrates that the high sparsity observed in controlled benchmarks translates directly to real-world deployment.

Several limitations apply. We study GRPO on single-turn reasoning tasks; other algorithms (PPO, DPO) may behave differently, though prior work [21] found comparable sparsity for RLHF. Our analysis assumes Adam-style optimizers; other optimizers may behave differently (Section A.6). Hyperparameters beyond learning rate (e.g., effective batch size) may also influence sparsity. Future work will extend this analysis to long-running post-training and multi-turn RL settings, where environment feedback may introduce novel token sequences that affect update sparsity.

By reducing synchronization costs by over 100 $\times$ , PULSE removes the communication bottleneck that has limited decentralized RL training, enabling geographically distributed networks to approach the iteration speed of centralized training.

## References

- [1] Long Ouyang, Jeff Wu, Xu Jiang, Diogo Almeida, Carroll L. Wainwright, Pamela Mishkin, Chong Zhang, Sandhini Agarwal, Katarina Slama, Alex Ray, et al. Training language models to follow instructions with human feedback. *Advances in Neural Information Processing Systems*, 35:27730–27744, 2022.
- [2] Paul F Christiano, Jan Leike, Tom B Brown, Miljan Martic, Shane Legg, and Dario Amodei. Deep reinforcement learning from human preferences. *Advances in Neural Information Processing Systems*, 30, 2017.
- [3] Nisan Stiennon, Long Ouyang, Jeff Wu, Daniel M Ziegler, Ryan Lowe, Chelsea Voss, Alec Radford, Dario Amodei, and Paul Christiano. Learning to summarize from human feedback. *Advances in Neural Information Processing Systems*, 33:3008–3021, 2020.
- [4] Yuntao Bai, Saurav Kadavath, Sandipan Kundu, Amanda Askell, Jackson Kernion, Andy Jones, Anna Chen, Anna Goldie, Azalia Mirhoseini, Cameron McKinnon, et al. Constitutional AI: Harmlessness from AI feedback. *arXiv preprint arXiv:2212.08073*, 2022.
- [5] Harrison Lee, Samrat Phatale, Hassan Mansoor, Thomas Mesnard, Johan Ferret, Kellie Lu, Colton Bishop, Ethan Hall, Victor Carbune, Abhinav Rastogi, and Sushant Prakash. RLAIF vs. RLHF: Scaling reinforcement learning from human feedback with AI feedback. In *Proceedings of the 41st International Conference on Machine Learning*, volume 235 of *Proceedings of Machine Learning Research*, pages 26874–26901. PMLR, 2024.
- [6] Zhihong Shao, Peiyi Wang, Qihao Zhu, Runxin Xu, Junxiao Song, Xiao Bi, Haowei Zhang, Mingchuan Zhang, Y.K. Li, Y. Wu, and Daya Guo. DeepSeekMath: Pushing the limits of mathematical reasoning in open language models. *arXiv preprint arXiv:2402.03300*, 2024.
- [7] DeepSeek-AI, Daya Guo, Dejian Yang, Haowei Zhang, Junxiao Song, Peiyi Wang, et al. DeepSeek-R1: Incentivizing reasoning capability in LLMs via reinforcement learning. *arXiv preprint arXiv:2501.12948*, 2025.
- [8] Saksham Sahai Srivastava and Vaneet Aggarwal. A technical survey of reinforcement learning techniques for large language models. *arXiv preprint arXiv:2507.04136*, 2025.
- [9] An Yang, Anfeng Li, Baosong Yang, Beichen Zhang, Binyuan Hui, Bo Zheng, et al. Qwen3 technical report. *arXiv preprint arXiv:2505.09388*, 2025.
- [10] Team OLMo et al. Olmo 3. *arXiv preprint arXiv:2512.13961*, 2025.
- [11] Gemini Team. Gemini 2.5: Pushing the frontier with advanced reasoning, multimodality, long context, and next generation agentic capabilities. *arXiv preprint arXiv:2507.06261*, 2025.
- [12] Jian Hu, Xibin Wu, Wei Shen, Jason Klein Liu, Zilin Zhu, Weixun Wang, Songlin Jiang, Haoran Wang, Hao Chen, Bin Chen, Weikai Fang, Xianyu, Yu Cao, Haotian Xu, and Yiming Liu. OpenRLHF: An easy-to-use, scalable and high-performance RLHF framework. *arXiv preprint arXiv:2405.11143*, 2024.
- [13] Guangming Sheng, Chi Zhang, Zilingfeng Ye, Xibin Wu, Wang Zhang, Ru Zhang, Yanghua Peng, Haibin Lin, and Chuan Wu. HybridFlow: A flexible and efficient RLHF framework. In *Twentieth European Conference on Computer Systems (EuroSys '25)*, 2025. doi: 10.1145/3689031.3696075.
- [14] Gerald Shen, Zhilin Wang, Olivier Delalleau, Jiaqi Zeng, Yi Dong, Daniel Egert, Shengyang Sun, Jimmy Zhang, Sahil Jain, Ali Taghibakhshi, Markel Sanz Ausin, Ashwath Aithal, and Oleksii Kuchaiev. NeMo-Aligner: Scalable toolkit for efficient model alignment. In *Conference on Language Modeling (COLM)*, 2024.
- [15] Prime Intellect Team, Sami Jaghouar, Justus Mattern, Jack Min Ong, Jannik Straube, Manveer Basra, Aaron Pazdera, Kushal Thaman, Matthew Di Ferrante, Felix Gabriel, Fares Obeid, Kemal Erdem, Michael Keiblanger, and Johannes Hagemann. INTELLECT-2: A reasoning model trained through globally decentralized reinforcement learning, 2025.

[16] Dan Alistarh, Demjan Grubic, Jerry Li, Ryota Tomioka, and Milan Vojnovic. QSGD: Communication-efficient SGD via gradient quantization and encoding. In *Advances in Neural Information Processing Systems*, volume 30, 2017.

[17] Yujun Lin, Song Han, Huizi Mao, Yu Wang, and William J Dally. Deep gradient compression: Reducing the communication bandwidth for distributed training. In *International Conference on Learning Representations*, 2018.

[18] Thijs Vogels, Sai Praneeth Karimireddy, and Martin Jaggi. PowerSGD: Practical low-rank gradient compression for distributed optimization. In *Advances in Neural Information Processing Systems*, volume 32, 2019.

[19] Amir Sarfi, Benjamin Thérien, Joel Lidin, and Eugene Belilovsky. Communication efficient LLM pre-training with SparseLoCo. *arXiv preprint arXiv:2508.15706*, 2025.

[20] Song Han, Huizi Mao, and William J Dally. Deep compression: Compressing deep neural networks with pruning, trained quantization and huffman coding. In *International Conference on Learning Representations*, 2016.

[21] Sagnik Mukherjee, Lifan Yuan, Dilek Hakkani-Tür, and Hao Peng. Reinforcement learning finetunes small subnetworks in large language models. In *Advances in Neural Information Processing Systems*, 2025. NeurIPS 2025.

[22] Qiying Yu et al. DAPO: An open-source LLM reinforcement learning system at scale. *arXiv preprint arXiv:2503.14476*, 2025.

[23] John Schulman, Filip Wolski, Prafulla Dhariwal, Alec Radford, and Oleg Klimov. Proximal policy optimization algorithms. *arXiv preprint arXiv:1707.06347*, 2017.

[24] Zichen Liu, Changyu Chen, Wenjun Li, Penghui Qi, Tianyu Pang, Chao Du, Wee Sun Lee, and Min Lin. Understanding R1-zero-like training: A critical perspective. *arXiv preprint arXiv:2503.20783*, 2025.

[25] Qwen Team. Qwen2.5 technical report. *arXiv preprint arXiv:2412.15115*, 2024.

[26] Aaron Grattafiori et al. The llama 3 herd of models. *arXiv preprint arXiv:2407.21783*, 2024.

[27] Gemma Team. Gemma 3 technical report. *arXiv preprint arXiv:2503.19786*, 2025.

[28] Dan Hendrycks, Collin Burns, Saurav Kadavath, Akul Arora, Steven Basart, Eric Tang, Dawn Song, and Jacob Steinhardt. Measuring mathematical problem solving with the MATH dataset. In *Advances in Neural Information Processing Systems (Datasets and Benchmarks Track)*, 2021.

[29] Devvrit Khatri, Lovish Madaan, Rishabh Tiwari, Rachit Bansal, Sai Surya Duvvuri, Manzil Zaheer, Inderjit S. Dhillon, David Brandfonbrener, and Rishabh Agarwal. The art of scaling reinforcement learning compute for LLMs. *arXiv preprint arXiv:2510.13786*, 2025.

[30] Idan Shenfeld, Jyothish Pari, and Pulkit Agrawal. RL's razor: Why online reinforcement learning forgets less. *arXiv preprint arXiv:2509.04259*, 2025.

[31] Hanqing Zhu, Zhenyu Zhang, Hanxian Huang, DiJia Su, Zechun Liu, Jiawei Zhao, Igor Fedorov, Hamed Pirsiavash, Zhizhou Sha, Jinwon Lee, David Z. Pan, Zhangyang Wang, Yuandong Tian, and Kai Sheng Tai. The path not taken: RLVR provably learns off the principals. *arXiv preprint arXiv:2511.08567*, 2025.

[32] Paulius Micikevicius, Sharan Narang, Jonah Alben, Gregory F. Diamos, Erich Elsen, David Garcia, Boris Ginsburg, Michael Houston, Oleksii Kuchaiev, Ganesh Venkatesh, and Hao Wu. Mixed precision training. In *International Conference on Learning Representations*, 2018.

[33] Erfan Miah. grail-v0: How we built a fully open, incentivized, decentralized reinforcement learning system. Templar Research Blog, 2025. URL <https://templarresearch.substack.com/p/grail-v0-how-we-built-a-fully-open>.

- [34] Jacob Austin, Augustus Odena, Maxwell Nye, Maarten Bosma, Henryk Michalewski, David Dohan, Ellen Jiang, Carrie Cai, Michael Terry, Quoc Le, and Charles Sutton. Program synthesis with large language models. *arXiv preprint arXiv:2108.07732*, 2021.
- [35] Hugo Touvron, Louis Martin, Kevin Stone, Peter Albert, Amjad Almahairi, Yasmine Babaei, Nikolay Bashlykov, Soumya Batra, Prajwäl Bhargava, Shruti Bhosale, et al. Llama 2: Open foundation and fine-tuned chat models. *arXiv preprint arXiv:2307.09288*, 2023.
- [36] DeepSeek-AI. DeepSeek-V3 technical report. *arXiv preprint arXiv:2412.19437*, 2024.
- [37] Team OLMo, Pete Walsh, Luca Soldaini, Dirk Groeneveld, Kyle Lo, Shane Arora, Akshita Bhagia, Yuling Gu, Shengyi Huang, Matt Jordan, Nathan Lambert, Dustin Schwenk, Oyvind Tafjord, et al. 2 OLMo 2 furious. *arXiv preprint arXiv:2501.00656*, 2025.
- [38] Leandro von Werra, Younes Belkada, Lewis Tunstall, Edward Beeching, Tristan Thrush, Nathan Lambert, Shengyi Huang, Kashif Rasul, and Quentin Gallouédec. TRL: Transformer reinforcement learning. <https://github.com/huggingface/trl>, 2020.

## A Theoretical Analysis

### A.1 Formal Sparsity Definitions

We provide formal definitions of the sparsity metrics used throughout this paper. These definitions quantify how many parameters change between training steps.

**Definition A.1** (Weight Update). Given model parameters  $\theta_t \in \mathbb{R}^d$  at optimization step  $t$  and parameters  $\theta_{t+k}$  at step  $t+k$ , the  **$k$ -step weight update** is:

$$\Delta_{t,k} = \theta_{t+k} - \theta_t \quad (2)$$

For consecutive steps ( $k = 1$ ), we simplify the notation to  $\Delta_t = \theta_{t+1} - \theta_t$ .

**Definition A.2** (Update Sparsity). The **sparsity** of a  $k$ -step weight update is the fraction of parameters that remain bitwise identical between step  $t$  and  $t+k$ :

$$S_k(t) = \frac{1}{d} \sum_{i=1}^d \mathbb{1}[\theta_{t+k}^{(i)} = \theta_t^{(i)}] \quad (3)$$

where  $\mathbb{1}[\cdot]$  is the indicator function. Equality is evaluated bitwise on the underlying representation (e.g., BF16). Higher values indicate fewer parameters changed, enabling greater compression.

The key insight exploited by PULSE is that  $S_1(t)$  is approximately 99% in RL fine-tuning (Section 3), enabling dramatic communication reduction.

### A.2 BF16 Precision and Update Absorption

BF16 (bfloat16) uses 1 sign bit, 8 exponent bits, and 7 mantissa bits. The 7-bit mantissa provides  $2^7 = 128$  distinct values between consecutive powers of two, making the smallest representable relative change approximately  $\epsilon_{\text{bf16}} = 2^{-7} \approx 0.0078$ .

Critically, this representable gap *scales with weight magnitude*. For example, between 1.0 and 2.0, the gap is 0.0078, but between 10.0 and 20.0, the gap is 0.078.

**Definition A.3** (Update Absorption). An optimizer update  $\Delta w$  to parameter  $w$  is *absorbed* if the BF16 representation remains unchanged:  $\text{bf16}(w + \Delta w) = \text{bf16}(w)$ . This occurs when the update is smaller than half the representable gap:

$$\frac{|\Delta w|}{|w|} < 2^{-8} = \frac{1}{256} \approx 0.004 \quad (4)$$

In mixed-precision training [32], the optimizer computes  $\Delta w$  in FP32, but the result is cast to BF16 when written to the weight tensor. If  $|\Delta w|$  is too small relative to  $|w|$ , the value rounds back to  $w$  and the update has no effect.

Figure 7 illustrates this mechanism. The key insight is that absorption depends on the *ratio*  $|\Delta w|/|w|$ , not  $|\Delta w|$  alone. Small weights can receive small updates; large weights cannot.

**Critical weight magnitude.** Combining the absorption threshold with Adam’s update rule yields a critical weight magnitude. In Adam,  $|\Delta w| \approx \eta$  for typical gradient patterns (see Section A.3 for formal analysis). For an update to survive, we need  $|\Delta w| > |w|/256$ , or:

$$|w| < 256 \cdot |\Delta w| \approx 256\eta \quad (5)$$

At learning rate  $\eta = 3 \times 10^{-6}$ , this gives  $|w|_{\text{crit}} \approx 7.7 \times 10^{-4}$ . Since typical LLM weights have magnitudes in  $[0.01, 1.0]$ , the vast majority exceed this threshold and are effectively frozen.

**Empirical validation with mixed-precision training.** The standard configuration for LLM post-training uses mixed-precision training [32]: the optimizer maintains FP32 master weights for numerical stability, while forward and backward passes execute in BF16. This differs fundamentally from pure FP32 training, where all computation and storage uses FP32 and sparsity is eliminated entirely [30].

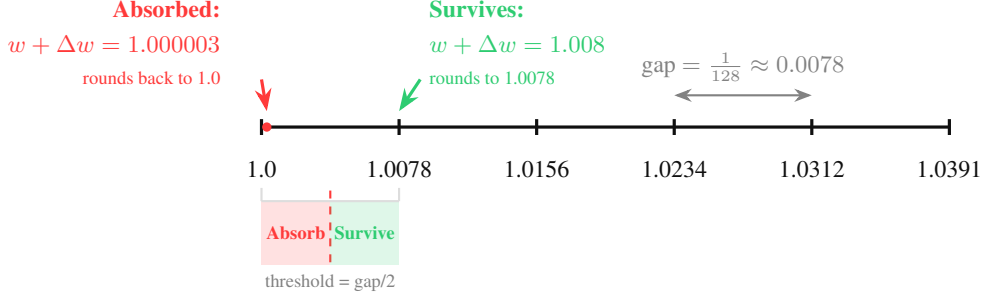


Figure 7: **Update absorption in BF16 arithmetic.** BF16 can represent only 128 distinct values between consecutive powers of two (shown as tick marks). Updates falling in the red zone round back to the original value and are absorbed; updates in the green zone survive. With learning rate  $3 \times 10^{-6}$  and weight  $w = 1.0$ , a typical update  $\Delta w \approx 3 \times 10^{-6}$  falls deep in the absorption zone (ratio  $3 \times 10^{-6} \ll 1/256$ ).

In mixed-precision training, although the optimizer updates FP32 master weights (where small updates *do* accumulate), inference still requires BF16 weights since all forward computation happens in BF16. Therefore, the relevant question for PULSE is: *how sparse are the weight updates when viewed in BF16?* We measure this by casting the FP32 master weights to BF16 after each optimization step and comparing consecutive BF16 snapshots. This reflects the actual weights that inference nodes receive and use.

Figure 8 validates that sparsity remains high under this standard setup. We train Qwen2.5-1.5B-Instruct with GRPO using FP32 master weights and BF16 computation; the resulting BF16-cast weight updates exhibit sparsity consistently above 99.4%, comparable to the pure BF16 results in Section 3.

This high sparsity persists because per-step updates are so small that even when accumulated in FP32, crossing the BF16 threshold requires many steps. At learning rate  $\eta = 3 \times 10^{-6}$ , a typical update magnitude is  $\sim \eta$ , while the BF16 threshold for a weight with  $|w| = 0.01$  is  $|w|/256 \approx 4 \times 10^{-5}$ . Since the threshold is roughly 13× larger than a single update, approximately 13 steps of consistent updates would be needed to cross it. Consequently, at any given step, only a small fraction of weights have accumulated enough change to affect their BF16 representation. Unlike pure BF16 training where absorbed updates are permanently lost, mixed-precision updates do eventually manifest, but spread across many steps, preserving high per-step sparsity. Practitioners using standard mixed-precision pipelines benefit from this sparsity without modification.

### A.3 Adam Update Bounds

We derive an upper bound on the per-step update magnitude in Adam. This bound, combined with the BF16 absorption threshold, characterizes which weights can be updated.

**Theorem A.4** (Adam Update Upper Bound). *For the Adam optimizer with parameters  $(\beta_1, \beta_2)$  where  $\beta_2 > \beta_1$ , the update magnitude at step  $t$  satisfies:*

$$|\Delta w_t| \leq \eta \sqrt{\frac{1 - \beta_1}{1 - \beta_2} \cdot \frac{1 - \beta_2^t}{1 - \beta_1^t}} \quad (6)$$

As  $t \rightarrow \infty$ , this simplifies to:

$$|\Delta w_t| \leq \eta \sqrt{\frac{1 - \beta_1}{1 - \beta_2}} \quad (7)$$

*Proof.* Let  $\Delta w_t = \eta \cdot \rho_t$  where  $\rho_t = \hat{m}_t / (\sqrt{\hat{v}_t} + \epsilon)$ . The bias-corrected EMA forms are:

$$\hat{m}_t = \sum_{i=1}^t p_i g_i, \quad \hat{v}_t = \sum_{i=1}^t q_i g_i^2 \quad (8)$$

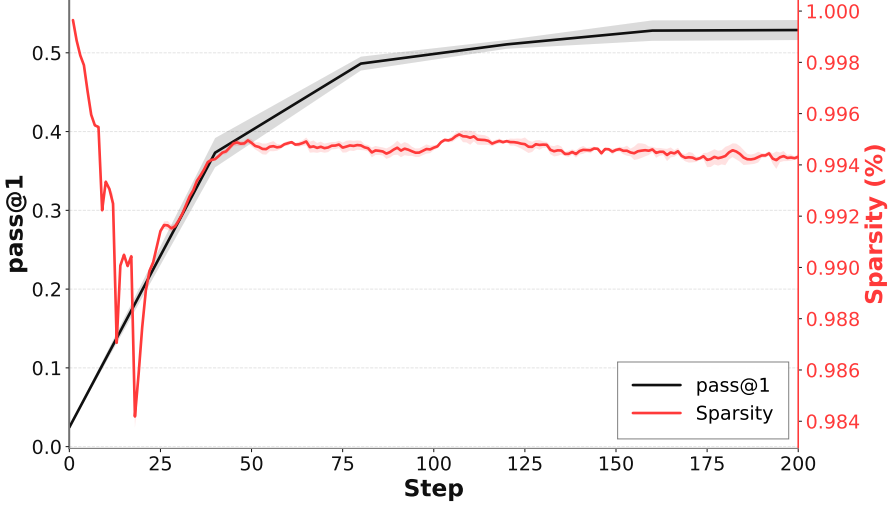


Figure 8: **Sparsity with mixed-precision training (FP32 master weights, BF16 computation).** Training Qwen2.5-1.5B-Instruct with GRPO on MATH tasks. Validation pass@1 improves steadily while weight update sparsity (measured by casting FP32 master weights to BF16 and comparing consecutive steps) remains consistently above 99.4%. Shaded regions indicate  $\pm 1$  standard deviation across 4 seeds.

where  $p_i, q_i \geq 0$  are the weights of the moving averages, with  $\sum_i p_i = \sum_i q_i = 1$ :

$$p_i = \frac{(1 - \beta_1)\beta_1^{t-i}}{1 - \beta_1^t}, \quad q_i = \frac{(1 - \beta_2)\beta_2^{t-i}}{1 - \beta_2^t} \quad (9)$$

Since  $\beta_2 > \beta_1$ , the ratio  $q_i/p_i$  is minimized at the most recent term  $i = t$ :

$$\frac{q_i}{p_i} \geq c_t \quad \text{for all } i, \quad \text{where } c_t = \frac{1 - \beta_2}{1 - \beta_1} \cdot \frac{1 - \beta_1^t}{1 - \beta_2^t} \quad (10)$$

By Jensen's inequality (since  $x^2$  is convex), we can bound the second moment:

$$\hat{v}_t = \sum_{i=1}^t q_i g_i^2 \geq c_t \sum_{i=1}^t p_i g_i^2 \quad (11)$$

$$\geq c_t \left( \sum_{i=1}^t p_i g_i \right)^2 = c_t \cdot \hat{m}_t^2 \quad (12)$$

Therefore:

$$\frac{|\hat{m}_t|}{\sqrt{\hat{v}_t}} \leq \frac{1}{\sqrt{c_t}} = \sqrt{\frac{1 - \beta_1}{1 - \beta_2} \cdot \frac{1 - \beta_1^t}{1 - \beta_2^t}} \quad (13)$$

Since  $\sqrt{\hat{v}_t} + \epsilon \geq \sqrt{\hat{v}_t}$ , we have  $|\rho_t| \leq 1/\sqrt{c_t}$ , completing the proof.  $\square$

**Validity of the condition  $\beta_2 > \beta_1$ .** The theorem requires  $\beta_2 > \beta_1$ , which holds universally across standard AdamW configurations. The choice of  $\beta_2 = 0.95$  (rather than the default 0.999) has become prevalent in modern LLM pre-training. This yields a tighter bound of  $\sqrt{(1 - 0.9)/(1 - 0.95)} = \sqrt{2} \approx 1.41$  compared to  $\sqrt{100} = 10$  for PyTorch defaults.

**Implications for standard hyperparameters.** For the PyTorch default parameters  $(\beta_1, \beta_2) = (0.9, 0.999)$ :

$$|\Delta w_t| \leq \eta \sqrt{\frac{0.1}{0.001}} = 10\eta \quad (14)$$

Table 1: AdamW hyperparameters used by major LLM training pipelines. All configurations satisfy  $\beta_2 > \beta_1$ .

Model / Framework	$\beta_1$	$\beta_2$	Asymptotic Bound	Reference
PyTorch default	0.9	0.999	$10\eta$	—
LLaMA 2/3	0.9	0.95	$\sqrt{2}\eta \approx 1.41\eta$	Grattafiori et al. [26], Touvron et al. [35]
DeepSeek-V3/R1	0.9	0.95	$\sqrt{2}\eta \approx 1.41\eta$	DeepSeek-AI [36]
Qwen 2.5	0.9	0.95	$\sqrt{2}\eta \approx 1.41\eta$	Qwen Team [25]
OLMo 2	0.9	0.95	$\sqrt{2}\eta \approx 1.41\eta$	Team OLMo et al. [37]
<b>This work</b>	0.9	0.99	$\sqrt{10}\eta \approx 3.16\eta$	Section C.2

Table 2: Weight magnitude statistics across model families. The critical threshold for update absorption at learning rate  $\eta = 3 \times 10^{-6}$  is  $|w|_{\text{crit}} \approx 7.7 \times 10^{-4}$  (typical, ratio  $\approx 1$ ). Weights above this threshold cannot receive updates in BF16, explaining the observed  $\sim 99\%$  per-step sparsity.

Model	Median $ w $	Mean $ w $	5th %ile	95th %ile	% $>  w _{\text{crit}}$
Qwen2.5-0.5B	0.0115	0.0147	0.0010	0.0381	96.3%
Qwen2.5-1.5B	0.0117	0.0150	0.0010	0.0389	96.3%
Qwen2.5-3B	0.0120	0.0153	0.0010	0.0396	96.4%
Qwen2.5-7B	0.0122	0.0156	0.0011	0.0404	96.5%
Llama-3.2-3B	0.0118	0.0151	0.0010	0.0392	96.4%
Gemma-3-4B	0.0121	0.0154	0.0011	0.0400	96.4%

With learning rate  $\eta = 3 \times 10^{-6}$ , this gives  $|\Delta w_t| \leq 3 \times 10^{-5}$ .

Table 1 summarizes the hyperparameters used by major LLM training pipelines. Modern LLM training often uses  $\beta_2 = 0.95$ , which yields a tighter bound of  $\sqrt{2}\eta \approx 1.41\eta$  compared to  $10\eta$  for the PyTorch default ( $\beta_2 = 0.999$ ).

**Corollary A.5** (Weight Magnitude Threshold for BF16). *For a weight  $w$  to receive a non-absorbed update in BF16 arithmetic, we require  $|\Delta w|/|w| > 2^{-8}$ . Combined with Theorem A.4, this gives the general bound:*

$$|w| < 256 \cdot |\Delta w|_{\text{max}} = 256\eta \sqrt{\frac{1 - \beta_1}{1 - \beta_2}} \quad (15)$$

For PyTorch defaults  $(\beta_1, \beta_2) = (0.9, 0.999)$ , this simplifies to  $|w| < 2560\eta$ . For modern LLM configurations with  $\beta_2 = 0.95$ , this becomes  $|w| < 362\eta$ . For our experimental setting  $(\beta_1, \beta_2) = (0.9, 0.99)$ , this gives  $|w| < 810\eta$ .

In practice, the ratio  $|\hat{m}_t|/\sqrt{\hat{v}_t} \approx 1$  for most gradient patterns (see Figure 9), yielding an effective threshold that is independent of  $\beta_2$ :

$$|w|_{\text{crit}}^{\text{effective}} < 256\eta \approx 7.68 \times 10^{-4} \quad (\text{for } \eta = 3 \times 10^{-6}) \quad (16)$$

This effective threshold determines practical sparsity, explaining why observed sparsity is consistent across different  $(\beta_1, \beta_2)$  configurations.

#### A.4 Weight Magnitude Distribution

To validate that the critical threshold  $|w|_{\text{crit}}$  is relevant to actual LLM weight distributions, we analyze weight magnitudes across several model families. Table 2 shows that the vast majority of LLM weights have magnitudes well above the critical threshold.

**Key observations.** The median weight magnitude across all models is approximately 0.011–0.012, which is roughly **15× larger** than the critical threshold  $|w|_{\text{crit}} \approx 7.7 \times 10^{-4}$ . This means that for typical Adam updates (ratio  $\approx 1$ ), approximately **96% of weights cannot receive updates** in BF16 arithmetic.

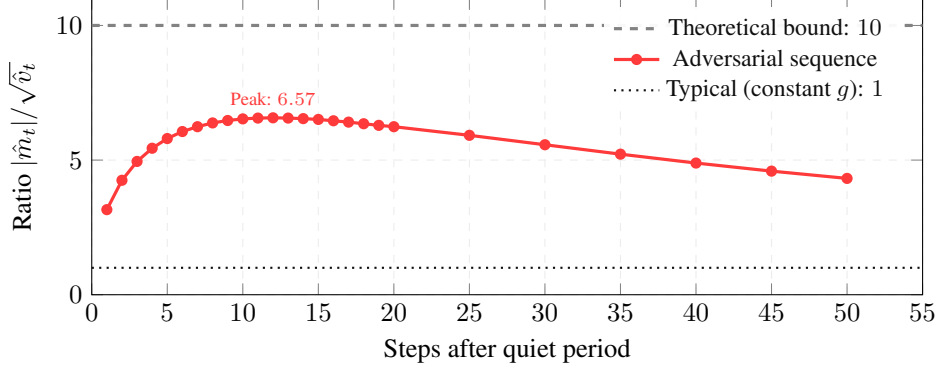


Figure 9: **Ratio  $|\hat{m}_t|/\sqrt{\hat{v}_t}$  for an adversarial gradient sequence.** The sequence consists of  $10^5$  near-zero gradients followed by constant gradients of magnitude 1. The ratio peaks at 6.57 after 12 large gradients, then decays as  $v_t$  catches up. Despite this extreme construction, the ratio only reaches 66% of the theoretical bound of 10. For constant gradients (typical case), the ratio equals 1.

**Connection to observed sparsity.** The theoretical prediction ( $\sim 96\%$  absorption based on weight magnitudes alone) is a lower bound; the empirically observed sparsity of  $\sim 99\%$  in Section 3 is higher due to additional factors:

- Some gradients producing updates with ratio  $> 1$ , allowing slightly more weights to be updated
- Numerical effects at boundary cases where  $|\Delta w| \approx |w|/256$

Figure 3 in the main text visualizes this relationship. The intersection of the BF16 threshold line with the Adam update bounds defines the critical weight magnitudes. Weights above these critical values (the vast majority) cannot receive updates, regardless of gradient magnitude.

**The bound is a supremum, not achievable by any single sequence.** The bound  $|\rho_t| \leq \sqrt{(1 - \beta_1)/(1 - \beta_2)}$  is a *supremum* over all possible gradient histories. It cannot be achieved by any single gradient sequence because the proof relies on Jensen’s inequality, which is tight only when all gradients are identical. However, if all gradients are identical ( $g_i = g$  for all  $i$ ), then  $\hat{m}_t = g$  and  $\hat{v}_t = g^2$ , yielding  $|\rho_t| = 1$ , not 10.

**Approaching the bound with adversarial sequences.** To understand how close we can get to the theoretical bound, consider the following adversarial gradient sequence: a long “quiet” period of near-zero gradients followed by constant large gradients. This exploits the fact that  $\beta_2 > \beta_1$  causes the second moment  $v_t$  to respond more slowly than the first moment  $m_t$ .

Figure 9 shows the ratio  $|\hat{m}_t|/\sqrt{\hat{v}_t}$  for the sequence  $[10^{-20}] \times 10^5 + [1.0] \times k$ . Key observations:

- The ratio peaks at **6.57** after 12 large gradients, only 66% of the theoretical bound
- After the peak,  $v_t$  accumulates and the ratio decays back toward 1
- For constant gradients (the typical case in training), the ratio equals exactly 1
- Even this highly adversarial sequence, which requires  $10^5$  steps of setup, cannot approach the bound

This analysis confirms that the bound of  $10\eta$  is extremely conservative. In practice, the ratio  $|\hat{m}_t|/\sqrt{\hat{v}_t}$  rarely exceeds 2 for realistic gradient sequences encountered during training.

## A.5 Conditions for Sparse Adam Updates

We systematically enumerate the conditions under which Adam optimizer updates become sparse (i.e., absorbed by BF16 precision). Recall that an update  $\Delta w$  is absorbed when  $|\Delta w| < |w|/256$ . The Adam update is:

$$\Delta w = \eta \cdot \frac{m_t}{\sqrt{v_t} + \epsilon} \quad (17)$$

Table 3: Conditions leading to sparse Adam updates in RL fine-tuning.

Condition	Mechanism	Prevalence
Small gradients ( $ g  \ll \epsilon$ )	Update numerator $\rightarrow 0$	Rare
Oscillating gradients	$m_t \rightarrow 0$ by cancellation	Moderate
Large weights ( $ w  > 10^{-3}$ )	BF16 threshold $ w /256$ too high	<b>Dominant</b>
Small learning rate ( $\eta = 3 \times 10^{-6}$ )	All updates scaled down	<b>Dominant</b>
High $\beta_2$ (0.999)	Persistent large $v_t$	Moderate

where  $m_t$  and  $v_t$  are the (bias-corrected) first and second moments,  $\eta$  is the learning rate, and  $\epsilon = 10^{-8}$ .

**Condition 1: Very small gradients ( $|g| \ll \epsilon$ ).** When gradients are extremely small (e.g.,  $|g| = 10^{-12}$ ), the update simplifies to  $|\Delta w| \approx \eta \cdot |g|/\epsilon$ . With  $\eta = 3 \times 10^{-6}$ ,  $|\Delta w| \approx 3 \times 10^{-10}$ , which is far below the absorption threshold for any weight magnitude.

**Condition 2: Oscillating gradients ( $m_t \rightarrow 0$ ,  $v_t$  grows).** When gradients oscillate around zero (e.g., alternating  $+g$  and  $-g$ ), the first moment  $m_t$  cancels while the second moment  $v_t$  accumulates ( $v_t \approx g^2$ ). This yields  $|\Delta w| \approx \eta \cdot 0/|g| \approx 0$ .

**Condition 3: Large weight magnitudes ( $|w| \gtrsim 10^{-2}$ ).** The BF16 absorption threshold scales with weight magnitude:  $|\Delta w|_{\min} = |w|/256$ . Even if the update is at its theoretical maximum ( $|\Delta w| \approx 10\eta$ ), large weights cannot be updated if  $|w| > 2560\eta$ . For  $\eta = 3 \times 10^{-6}$ , weights with  $|w| > 7.68 \times 10^{-3}$  are effectively frozen.

**Condition 4: Small learning rate.** The learning rate  $\eta$  directly scales all updates. Standard GRPO learning rates ( $\eta = 3 \times 10^{-6}$ ) are 100–1000× smaller than typical pre-training rates, reducing update magnitudes proportionally.

**Condition 5: High  $\beta_2$  (slow second moment decay).** With high  $\beta_2$  (e.g., 0.999), the second moment  $v_t$  decays very slowly. A parameter that experienced large gradients in the past will have an inflated  $v_t$ , suppressing future updates even if current gradients are moderate.

**Summary.** Table 3 summarizes these factors. The dominant drivers of sparsity in RL fine-tuning are **large weight magnitudes** and **small learning rates**, which interact with BF16 precision to produce ~99% per-step sparsity.

## A.6 Optimizer Dependence

The sparsity analysis throughout this paper assumes Adam-style optimizers. This choice is not incidental: Adam’s adaptive scaling fundamentally changes how gradient magnitudes translate to update magnitudes, making sparsity robust in ways that would not hold for SGD.

**Adam vs. SGD update dynamics.** In SGD, the update is  $\Delta w = \eta g$ , so update magnitude scales directly with gradient magnitude. Large gradients produce large updates that may exceed the BF16 absorption threshold. In contrast, Adam computes  $\Delta w = \eta \cdot \hat{m}_t / (\sqrt{\hat{v}_t} + \epsilon)$ , where both  $\hat{m}_t$  and  $\hat{v}_t$  track gradient statistics. When gradients are consistently large, both the first moment  $m_t$  and second moment  $v_t$  grow proportionally, keeping their ratio bounded near 1 (Figure 9). This normalization effect means that Adam’s update magnitude is largely independent of gradient magnitude.

**Upper bounds on updates.** A key distinction emerges when gradient clipping is disabled or ineffective. Adam has a theoretical upper bound on update magnitude regardless of gradient size:  $|\Delta w| \leq 10\eta$  for standard hyperparameters (Theorem A.4). SGD has no such bound;  $|\Delta w| = \eta|g|$  grows without limit as  $|g|$  increases. For example, with  $\eta = 3 \times 10^{-6}$  and an unclipped gradient  $|g| = 100$ :

- **Adam:**  $|\Delta w| \leq 10\eta = 3 \times 10^{-5}$  (bounded)
- **SGD:**  $|\Delta w| = \eta|g| = 3 \times 10^{-4}$  ( $10\times$  larger, exceeds BF16 threshold for more weights)

This bound makes Adam’s sparsity predictable: even under extreme gradient conditions, updates remain  $\mathcal{O}(\eta)$ .

**Implications for sparsity.** In practice, layer normalization and gradient clipping constrain gradient magnitudes. With clipping at global norm 1.0, per-parameter gradients are often  $|g| \leq 1$ , which means SGD updates ( $\eta|g|$ ) may be smaller than Adam updates ( $\sim\eta$ ), potentially yielding comparable or even higher sparsity. However, without clipping or when gradients spike, SGD’s unbounded updates could significantly reduce sparsity. We have not empirically verified sparsity under SGD; our analysis assumes Adam throughout.

**Practical relevance.** Since modern LLM training universally uses Adam variants (AdamW, Adam with decoupled weight decay), this distinction is primarily of theoretical interest. However, practitioners considering alternative optimizers (e.g., SGD with momentum for specific fine-tuning regimes) should be aware that the sparsity guarantees established in this paper may not transfer.

## A.7 Lossless Reconstruction Guarantee

PULSE guarantees bit-exact reconstruction because it stores *actual weight values* rather than arithmetic differences.

**Proposition A.6** (Lossless Reconstruction). *For any patch  $P = (\mathcal{I}, \mathcal{V})$  derived from consecutive checkpoints  $W_{t-1}$  and  $W_t$ , applying  $P$  to  $W_{t-1}$  reconstructs  $W_t$  exactly:*

$$\text{DECODE}(W_{t-1}, P) \equiv W_t \quad (\text{bitwise}) \quad (18)$$

*This property extends to chains of patches: applying  $P_1, P_2, \dots, P_n$  sequentially to anchor  $W_0$  reconstructs  $W_n$  exactly.*

The proof is immediate from the algorithm construction (Algorithm 1). Reconstruction performs direct memory assignment  $W[\mathcal{I}] \leftarrow \mathcal{V}$  with no floating-point arithmetic, as illustrated in Figure 10. For indices  $i \in \mathcal{I}$ , we copy the exact bit pattern from  $\mathcal{V}$ ; for indices  $i \notin \mathcal{I}$ , the value is unchanged and already correct. No rounding, truncation, or approximation occurs at any step.

**Contrast with additive delta schemes.** Traditional delta compression stores  $\delta_t = W_t - W_{t-1}$  and reconstructs via  $W_t = W_{t-1} + \delta_t$ . This addition is a floating-point operation subject to rounding. Over long chains, small errors accumulate:

$$W_{\text{recon}} = W_0 + \sum_{i=1}^n \delta_i \neq W_n \quad (\text{in general}) \quad (19)$$

PULSE avoids this entirely by storing values, not differences. Each patch application overwrites positions with their correct final values, independent of chain length.

**Practical verification.** We verify losslessness empirically via SHA-256 hashes. Each patch includes a hash of the expected reconstructed weights; inference nodes verify this hash after applying each patch. In all experiments (Section 5), 100% of reconstructions passed verification, confirming bit-identical weights across the network.

## B The grail Framework

We deploy PULSE on grail [33], a decentralized reinforcement learning platform built on Bittensor. This section summarizes grail’s asynchronous architecture; for complete implementation details, see the open-source repository.<sup>4</sup>

---

<sup>4</sup><https://github.com/one-covenant/grail>

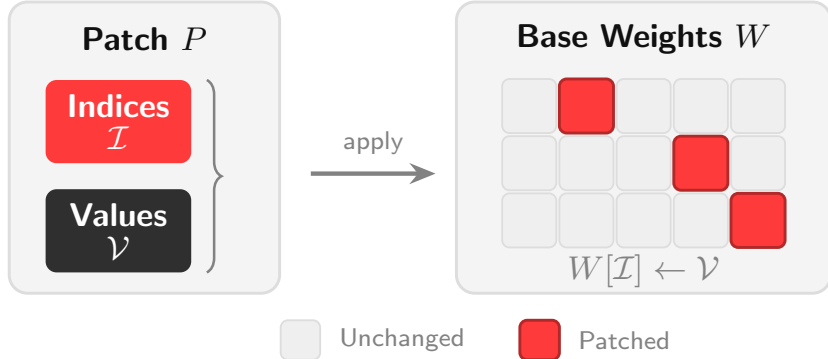


Figure 10: **Sparse value patching.** A patch  $P = (\mathcal{I}, \mathcal{V})$  consists of changed indices  $\mathcal{I}$  and their new values  $\mathcal{V}$ . To reconstruct  $W_t$  from  $W_{t-1}$ , we overwrite:  $W_t[\mathcal{I}] \leftarrow \mathcal{V}$ . This direct assignment requires no floating-point arithmetic, guaranteeing bit-exact reconstruction.

## B.1 System Overview

grail separates computationally expensive inference (rollout generation) from training, enabling distributed nodes to contribute compute while a centralized trainer handles gradient updates. The system comprises three node types:

- **Miners:** Generate inference rollouts using the current model checkpoint.
- **Validators:** Verify rollout authenticity via hidden-state fingerprinting and assign performance-based rewards.
- **Trainer:** Consumes verified rollouts to update the model.

All coordination occurs through S3-compatible object storage (e.g., Cloudflare R2), which serves as the shared layer for checkpoints and rollout data.

## B.2 Asynchronous Training Architecture

grail employs a fully asynchronous design where the trainer runs continuously without synchronization stalls. Miners and the trainer synchronize only at *window boundaries* (approximately every 6 minutes), but the trainer never blocks. Instead, it continuously samples from a replay buffer while dedicated background processes handle all I/O.

**Trainer node processes.** The trainer node runs three concurrent processes:

1. **Training process:** Executes a tight loop that samples batches from the replay buffer and performs gradient updates. This process never waits for I/O, enabling multiple updates per window.
2. **Upload process:** Handles checkpoint serialization and upload asynchronously. When the trainer produces a new checkpoint, it is handed off to this process without blocking.
3. **Download process:** Fetches verified rollouts from storage at window boundaries and adds them to the replay buffer with staleness metadata.

**Replay buffer.** The replay buffer decouples data arrival from training consumption. It stores rollouts from multiple windows, supports staleness-weighted sampling (preferring fresher data), and implements automatic eviction of stale entries. This design ensures the trainer always has data available, even during network delays.

### B.3 Rollout Verification

Validators verify that rollouts originate from the correct model checkpoint using a lightweight cryptographic mechanism called *grail Proof*:

- Select the top-32 hidden-state dimensions per token.
- Apply logarithmic quantization to handle heavy-tailed activation distributions.
- Generate 4-byte cryptographic sketches per token ( $\sim 148$  bits of security).
- Use adaptive tolerances to account for numerical drift across different hardware.

This verification ensures that miners cannot submit rollouts generated from outdated or modified checkpoints.

## C Experimental Details

### C.1 Hardware Configuration

We use different hardware configurations for the sparsity analysis (Section 3) and the distributed synchronization experiments (Section 4).

**Sparsity analysis (Section 3).** For the controlled sparsity experiments, we use two NVIDIA A100 80GB GPUs: one for training and one for inference/evaluation. This setup ensures reproducible measurements of weight update sparsity across different model sizes and training configurations.

**Distributed synchronization (Section 4).** For the distributed deployment experiments, the trainer process runs on a single NVIDIA H200 GPU. The inference nodes are fully decentralized and anonymous, participating voluntarily in the network without disclosing their hardware specifications. The network bandwidth between the trainer and inference nodes is approximately 400 Mb/s. Storage uses S3-compatible object storage for checkpoint distribution.

### C.2 Training Hyperparameters

We adopt standard GRPO configurations as summarized in Table 4. To ensure our sparsity analysis captures the *intrinsic* behavior of the optimization process, we set weight decay and the KL penalty  $\beta$  to zero during primary measurements.

Table 4: Training hyperparameters for GRPO experiments. These are the default values used in the sparsity analysis (Section 3). The decentralized experiments (Section 5) use a lower learning rate of  $1 \times 10^{-6}$ .

Parameter	Value
Optimizer	AdamW
Learning rate ( $\eta$ )	$3 \times 10^{-6}$
$(\beta_1, \beta_2)$	(0.9, 0.99)
Weight decay	0.0
LR schedule	Constant
Gradient clipping	1.0
GRPO clipping $\epsilon$	0.2
KL penalty $\beta$	0.0
Prompts per batch	64
Rollouts per prompt ( $G$ )	8
Max generation length	2048
Precision	BF16

### C.3 Reward Formulations

We use verifiable rewards for both mathematical reasoning and code generation tasks.

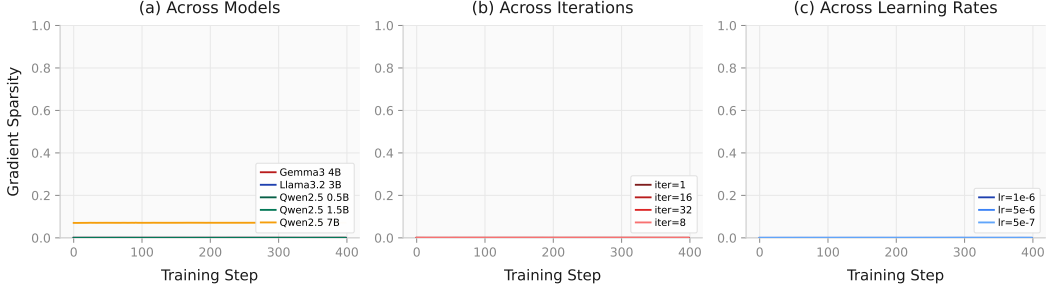


Figure 11: **Gradient sparsity throughout training for standard GRPO** across (a) model architectures and sizes, (b) iteration counts, and (c) learning rates. Sparsity is measured as the fraction of exactly-zero gradient values. Shaded regions indicate standard error across 4 seeds. Gradient sparsity remains near zero (<1%) throughout training regardless of model, iteration count, or learning rate, demonstrating that standard reinforcement learning produces dense gradients unsuitable for efficient communication in distributed training.

**Mathematical Reasoning (MATH).** For math tasks, we use a composite reward with four components: correctness (70% weight), answer format (15% weight), thinking presence (10% weight), and no-trailing penalty (5% weight):

$$R_{\text{math}} = 0.7 \cdot C_{\text{correct}} + 0.15 \cdot F_{\text{format}} + 0.1 \cdot T_{\text{thinking}} + 0.05 \cdot P_{\text{no-trailing}} \quad (20)$$

where  $C_{\text{correct}} \in [0, 1]$  is verified by string matching the final answer after normalization.

**Code Generation (MBPP).** For code generation tasks, we use a composite reward based on test pass rates (70% weight), syntax validity (10% weight), solution format (10% weight), and thinking presence (10% weight):

$$R_{\text{code}} = 0.7 \cdot C_{\text{pass}} + 0.1 \cdot S_{\text{valid}} + 0.1 \cdot F_{\text{format}} + 0.1 \cdot T_{\text{thinking}} \quad (21)$$

where  $C_{\text{pass}}$  is the fraction of unit tests passed by the generated code.

## C.4 Software Environment

The sparsity analysis (Section 3) uses TRL [38] for GRPO training. The decentralized experiments (Section 5) use grail [33], which integrates PULSE for sparse checkpoint synchronization.

```
Python: 3.10.12
PyTorch: 2.2.0
CUDA: 12.1
transformers: 4.38.0
zstandard: 0.22.0
```

## D Extended Results

### D.1 Gradient vs. Parameter Change Sparsity

To understand the mechanistic source of parameter sparsity, we separately analyze gradient sparsity before the optimizer processes them.

Gradients are nearly fully dense (~99% non-zero), yet parameter updates are highly sparse (~97% unchanged). Figure 11 visualizes this behavior across a wide range of training configurations, confirming that dense gradients are a universal property of standard GRPO. The BF16 absorption mechanism (Section 3.3.1) explains the transformation from dense gradients to sparse weight updates: dense gradients produce updates that fall below the representable threshold for most parameters.

This has practical implications for system design. Gradient compression techniques [16, 17] would achieve far lower compression ratios than parameter change compression, since gradients remain dense throughout training.

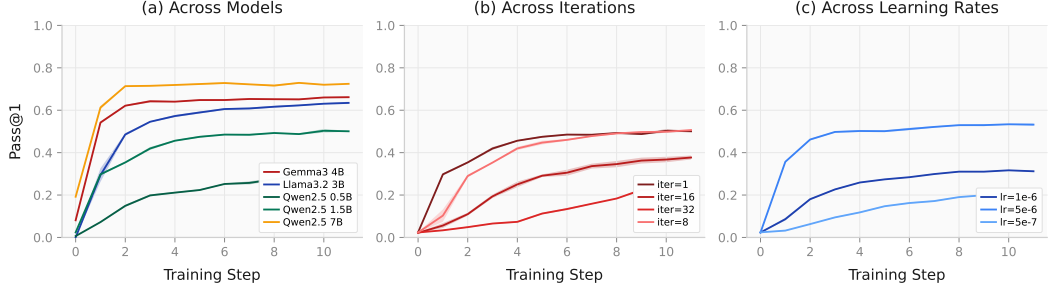


Figure 12: **Training curves across model scales.** Pass@1 validation accuracy throughout training for all models used in our sparsity analysis. All models show rapid initial improvement followed by convergence within 400 steps, validating our choice of training duration. Shaded regions indicate  $\pm 1$  standard error across 4 seeds.

## D.2 Training Curves Across Model Scales

To validate that our 400-step training duration captures the meaningful learning dynamics, we present pass@1 accuracy curves across all model families and sizes used in our sparsity analysis.

Figure 12 shows that all models exhibit similar learning dynamics: rapid initial improvement in the first 100–200 steps, followed by gradual convergence. By step 400, performance has largely plateaued across all model scales and families, confirming that our experimental duration is sufficient to capture stable-phase sparsity behavior. This consistency across architectures (Qwen, Llama, Gemma) and scales (0.5B–7B) provides confidence that our sparsity observations reflect the converged training regime rather than transient early-training artifacts.

## E Method Details

### E.1 GRPO Formulation

GRPO eliminates the need for a separate value network by estimating advantages from group-relative rewards. Following DAPO [22], we use asymmetric clipping bounds  $\epsilon_{\text{low}}$  and  $\epsilon_{\text{high}}$  to encourage exploration. The objective function is:

$$\mathcal{J}_{\text{GRPO}}(\theta) = \mathbb{E}_{x \sim \mathcal{D}, \{y_i\}_{i=1}^G \sim \pi_{\theta_{\text{old}}}(\cdot|x)} \left[ \frac{1}{G} \sum_{i=1}^G \frac{1}{|y_i|} \sum_{t=1}^{|y_i|} \left\{ \min \left[ r_{i,t}(\theta) \hat{A}_i, \text{clip}(r_{i,t}(\theta), 1-\epsilon_{\text{low}}, 1+\epsilon_{\text{high}}) \hat{A}_i \right] \right. \right. \\ \left. \left. - \beta D_{\text{KL}}[\pi_{\theta} \parallel \pi_{\text{ref}}] \right\} \right] \quad (22)$$

where  $\{y_i\}_{i=1}^G$  are  $G$  sampled responses for a given prompt  $x$ , and the importance weight ratio is:

$$r_{i,t}(\theta) = \frac{\pi_{\theta}(y_{i,t}|x, y_{i,<t})}{\pi_{\theta_{\text{old}}}(y_{i,t}|x, y_{i,<t})} \quad (23)$$

The advantage  $\hat{A}_i$  for the  $i$ -th response is computed relative to the group statistics:

$$\hat{A}_i = \frac{r(x, y_i) - \mu_G}{\sigma_G}, \quad \text{where} \quad \mu_G = \frac{1}{G} \sum_{j=1}^G r(x, y_j), \quad \sigma_G = \sqrt{\frac{1}{G} \sum_{j=1}^G (r(x, y_j) - \mu_G)^2} \quad (24)$$

The clipping mechanism prevents overly large policy updates, with the asymmetric bounds ( $\epsilon_{\text{high}} > \epsilon_{\text{low}}$ ) relaxing the upper limit to mitigate entropy collapse. The KL penalty (controlled by  $\beta$ ) regularizes deviations from the reference policy  $\pi_{\text{ref}}$ .

Table 5: **Component contribution to compression ratio.** Each row adds one transformation. Sparse ratio is relative to COO baseline;  $\Delta$  shows incremental improvement. All measurements use zstd-1 ( $n = 270$ ).

Configuration	Sparse Ratio	$\Delta$ Ratio	Encode (MB/s)
Raw COO (baseline)	$2.71 \times \pm 0.25$	–	397
+ Index sorting	$2.71 \times \pm 0.25$	+0.0%	397
+ Delta encoding	$3.07 \times \pm 0.34$	+13.3%	398
+ Type downscaling	$3.33 \times \pm 0.29$	+8.5%	534

## E.2 Index Encoding

We use delta encoding for indices to improve compression:

1. Sort indices in ascending order
2. Store first index as-is (4 bytes)
3. Store subsequent indices as differences from previous
4. Use variable-length encoding for differences

This typically reduces index storage by 40–60% before zstd compression.

## E.3 Memory Management

The PULSE method requires maintaining the previous checkpoint to compute the sparse delta. The memory overhead is minimal:

- **Training node:** Maintains the current weights on the GPU and the previous weights in pinned CPU memory. This results in a total memory overhead of approximately  $1.1 \times$  the model size compared to standard training.
- **Inference node:** Loads the base weights once and applies incoming deltas in-place. No additional weight copies are required after the initial load.

## E.4 Compression Ablation Study

This section provides comprehensive ablation studies for the compression pipeline summarized in Section 3.4. We analyze: (1) component contributions to compression ratio, (2) sparse representation format choices, (3) full algorithm comparison with Pareto analysis, and (4) per-model variations.

**Methodology.** We measured compression performance on sparse delta checkpoints from 14 experiments across 3 model families (Qwen2.5, Gemma3, LLaMA3.2), with 20 checkpoint files per experiment (5 evenly-spaced steps  $\times$  4 seeds). We tested 6 sparse representations  $\times$  5 compression algorithms = 30 combinations, yielding 8,100 total measurements. Timing measurements used 1 warmup + 3 measurement iterations on an AMD EPYC 7763 processor, with verification that  $\text{decompress}(\text{compress}(x)) == x$  for all.

**Compression ratio definition.** Throughout this section, *sparse ratio* refers to compression of the sparse representation itself (compressed bytes / COO baseline bytes), while *full ratio* refers to compression versus the dense BF16 model (dense bytes / compressed bytes).

### E.4.1 Component Contribution Analysis

The compression pipeline applies several transformations before entropy coding. Table 5 shows the incremental contribution of each component using zstd-1 across all models ( $n = 270$ ).

**Index sorting.** Sorting indices in ascending order has no direct size impact but enables delta encoding.

Table 6: **Sparse representation format comparison** using int32 indices and zstd-1 ( $n = 270$ ).

Format	Sparse Ratio	Encode (MB/s)
2D COO (delta_coo_int32)	$3.07 \times \pm 0.34$	398
1D Flat (delta_flat_int32)	$3.19 \times \pm 0.29$	312

Table 7: **Compression algorithm comparison** using our default representation ( $n = 270$ ). Sparse ratio is vs COO baseline; full ratio is vs dense BF16 model.

Algorithm	Sparse Ratio	Full Ratio	Encode (MB/s)	Decode (MB/s)	Pareto
snappy	$2.41 \times \pm 0.15$	56 $\times$	$1041 \pm 357$	$1289 \pm 485$	*
lz4	$2.40 \times \pm 0.13$	56 $\times$	$830 \pm 236$	$1484 \pm 524$	*
<b>zstd-1</b>	<b><math>3.33 \times \pm 0.29</math></b>	<b>79<math>\times</math></b>	<b><math>534 \pm 56</math></b>	<b><math>851 \pm 108</math></b>	*
zstd-3	$3.40 \times \pm 0.27$	80 $\times$	$197 \pm 21$	$670 \pm 69$	*
gzip-6	$3.32 \times \pm 0.26$	78 $\times$	$14 \pm 2$	$192 \pm 11$	

**Delta encoding.** Instead of storing absolute indices, we store the first index and subsequent differences. Since changed parameters tend to cluster, differences are small and compress well. This contributes +13.3% improvement.

**Type downscaling.** For COO format, we store row deltas as uint8 and column deltas as uint16, exploiting the fact that consecutive changes rarely span more than 255 rows or 65,536 columns. This contributes an additional +8.5% improvement and also increases encode throughput (smaller data to process).

**Total improvement.** The full pipeline (delta encoding + downscaling) improves sparse compression ratio by +22.9% over the raw baseline ( $2.71 \times \rightarrow 3.33 \times$ ).

#### E.4.2 Sparse Representation Format Comparison

We compared two sparse representation strategies: (1) **2D COO**: store per-tensor (row, column) coordinates; (2) **1D Flat**: flatten all tensors, store global indices. Table 6 shows results with fair comparison (both using int32 indices).

**Finding.** 1D Flat achieves +3.9% better compression than 2D COO when using identical index types, because global indices enable better delta encoding across tensor boundaries. However, 2D COO enables type downscaling (uint8 row deltas, uint16 column deltas) which is harder for flat indices. Our default configuration uses COO with downscaling ( $3.33 \times$ ), which outperforms flat with int32 ( $3.19 \times$ ).

#### E.4.3 Full Algorithm Comparison

Table 7 compares compression algorithms using our default representation (delta\_coo\_downscaled). We mark Pareto-optimal configurations.

##### Key observations.

- **gzip-6 is never Pareto-optimal:** zstd-1 achieves the same ratio ( $3.33 \times$  vs  $3.32 \times$ ) but encodes  $38 \times$  faster (534 vs 14 MB/s).
- **snappy/lz4 for speed:** At high bandwidth, snappy (1041 MB/s) or lz4 (830 MB/s) minimize total transfer time despite lower ratios.
- **zstd dominates mid-range:** zstd-1 provides the best tradeoff for typical cloud bandwidths (15 Mbit/s–1 Gbit/s).

#### E.4.4 Per-Model Breakdown

Table 8 shows compression varies across model families.

Table 8: **Per-model compression** with zstd-1 default configuration.

Model Family	Sparsity	Sparse Ratio	Full Ratio	$n$
Qwen2.5 (0.5B–7B)	$99.0\% \pm 0.7\%$	$3.31 \times \pm 0.31$	$76\times$	210
LLaMA3.2 (3B)	$99.3\% \pm 0.1\%$	$3.36 \times \pm 0.18$	$100\times$	20
Gemma-3-4B	$99.2\% \pm 0.2\%$	$3.42 \times \pm 0.21$	$80\times$	40

**Observations.** LLaMA3.2 achieves the highest full compression ratio ( $100\times$ ) due to its high sparsity (99.3%) and favorable weight distribution. The measured range of  $76$ – $100\times$  across model families is consistent with the theoretical expectation: higher sparsity yields higher compression. The variation reflects differences in both sparsity levels and weight value distributions across architectures.

#### E.4.5 Bandwidth-Dependent Algorithm Selection

The optimal algorithm depends on bandwidth. Total transfer time is:

$$T_{\text{total}} = T_{\text{encode}} + \frac{S_{\text{payload}}}{R \cdot B} + T_{\text{decode}} \quad (25)$$

where  $S_{\text{payload}}$  is uncompressed sparse payload size,  $R$  is compression ratio, and  $B$  is bandwidth. At high  $B$ , encoding time dominates; at low  $B$ , transfer time dominates. Figure 13 visualizes this selection process across different bandwidth tiers.

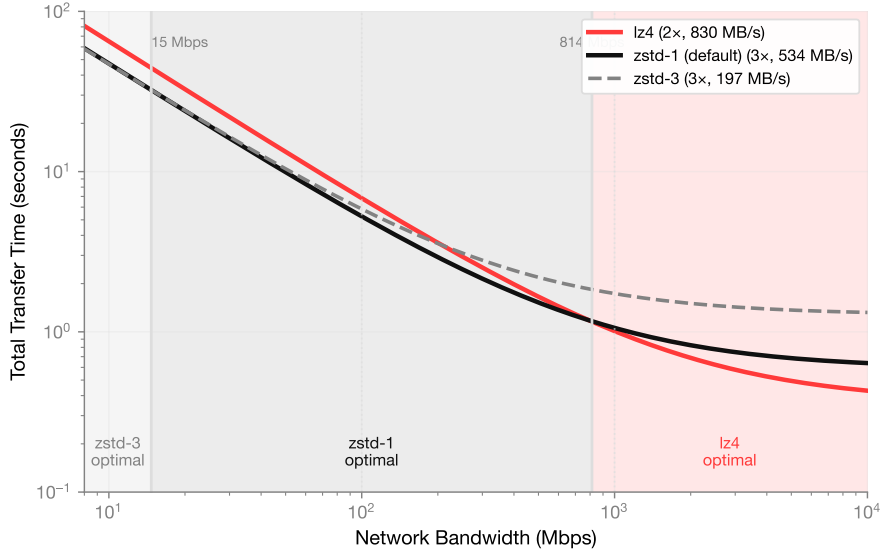


Figure 13: **Bandwidth-aware algorithm selection.** Total transfer time (encode + network + decode) for a 7B model. Shaded regions indicate the optimal algorithm per bandwidth tier. Fast algorithms like lz4 are preferred at high bandwidth, while high-ratio algorithms like zstd-3 are better for constrained links.

**Crossover formula.** The crossover bandwidth where two algorithms  $A$  and  $B$  have equal total transfer time can be derived analytically. Setting  $T_A = T_B$  and solving for bandwidth:

$$B_{\text{crossover}} = \frac{S_{\text{payload}} \cdot (R_A^{-1} - R_B^{-1})}{(T_{\text{enc},A} + T_{\text{dec},A}) - (T_{\text{enc},B} + T_{\text{dec},B})} \quad (26)$$

**Crossover points.** From our empirical benchmarks (194 MB payload, default configuration):

- **zstd-3 → zstd-1:**  $\sim 15$  Mb/s (below this, zstd-3's marginally better ratio wins)
- **zstd-1 → lz4:**  $\sim 800$  Mb/s (above this, lz4's faster encode wins)

These crossovers scale with payload size; larger payloads shift crossovers to higher bandwidths.

---

**Algorithm 2** Sparse Delta Encoding

---

**Require:** Current weights  $W_t$ , previous weights  $W_{t-1}$   
**Ensure:** Sparse delta  $\Delta = (\mathcal{I}, \mathcal{V}, \mathcal{S})$ , hash  $h$

```
1:  $\mathcal{I} \leftarrow \emptyset; \mathcal{V} \leftarrow \emptyset; \mathcal{S} \leftarrow \emptyset$ 
2: for each parameter tensor  $p \in \text{params}(W_t)$  do
3:    $\mathcal{M} \leftarrow \{i : W_t[p]_i \neq W_{t-1}[p]_i\}$                                  $\triangleright$  Find changed positions (bitwise)
4:   if  $|\mathcal{M}| > 0$  then
5:      $\mathcal{I}[p] \leftarrow \mathcal{M}; \mathcal{V}[p] \leftarrow W_t[p][\mathcal{M}]; \mathcal{S}[p] \leftarrow \text{shape}(W_t[p])$ 
6:   end if
7: end for
8:  $\Delta \leftarrow \text{COMPRESS}((\mathcal{I}, \mathcal{V}, \mathcal{S})); h \leftarrow \text{SHA256}(W_t)$ 
9: return  $\Delta, h$ 
```

---

---

**Algorithm 3** Sparse Delta Application

---

**Require:** Base weights  $W_{\text{base}}$ , sparse delta  $\Delta = (\mathcal{I}, \mathcal{V}, \mathcal{S})$   
**Ensure:** Reconstructed weights  $W_{\text{recon}}$

```
1:  $W_{\text{recon}} \leftarrow \text{COPY}(W_{\text{base}})$ 
2: for each parameter  $p$  with changes in  $\Delta$  do
3:    $W_{\text{recon}}[p][\mathcal{I}[p]] \leftarrow \mathcal{V}[p]$                                  $\triangleright$  Direct value assignment
4: end for
5: return  $W_{\text{recon}}$ 
```

---

**Why zstd-1 is the default.** Most deployments operate in the 15–800 Mb/s range (commodity internet, cross-datacenter links). In this regime, zstd-1 minimizes end-to-end latency while achieving 79 $\times$  full compression. Users with different bandwidth profiles can override via configuration.

## E.5 Algorithms

## F Comparison with Related Methods

Key differences from gradient compression: (1) we operate on weight differences, not gradients before aggregation; (2) our approach is lossless; (3) we exploit domain-specific structure (RL sparsity) rather than generic compression.

Our key innovation is storing actual values rather than differences, which enables lossless multi-hop reconstruction.

## G Distributed Synchronization Details

This section provides implementation details for the distributed synchronization protocol described in Section 4.2. We cover: (1) the formal synchronization protocol, (2) how to choose the anchor interval, (3) integrity verification mechanisms, (4) failure recovery strategies, (5) end-to-end latency analysis, (6) storage format specification, and (7) retention policies.

### G.1 Distributed Synchronization Protocol

The PULSE synchronization protocol operates asynchronously between training and inference nodes. Training nodes *publish* checkpoints to shared storage, while inference nodes independently *pull* updates. This decoupled design allows training and inference to scale independently.

Algorithm 4 formalizes the protocol. The key parameters are:  $W_t$  (weights at step  $t$ ),  $k$  (anchor interval), and  $h_t$  (integrity hash). The protocol distinguishes between a *fast path* (single delta application) and a *slow path* (anchor download plus delta chain).

---

**Algorithm 4** Distributed Synchronization Protocol

---

**Training Node (Publisher):**

```

1: procedure PUBLISHCHECKPOINT( $W_t, W_{t-1}, t, k$ )
2:    $h_t \leftarrow \text{SHA256}(W_t)$                                  $\triangleright$  Compute integrity hash
3:   if  $t \bmod k = 0$  then                                 $\triangleright$  Anchor window
4:     UPLOADFULL( $W_t, t, h_t$ )                                 $\triangleright$  Full checkpoint
5:      $W_{\text{anchor}} \leftarrow W_t; t_{\text{anchor}} \leftarrow t$ 
6:   end if
7:    $P \leftarrow \text{ENCODE}(W_t, W_{t-1})$                                  $\triangleright$  Sparse patch
8:   UPLOADDELTA( $P, t, t-1, t_{\text{anchor}}, h_t$ )
9:   SETREADYMARKER( $t$ )                                          $\triangleright$  Signal availability
10: end procedure

```

**Inference Node (Consumer):**

```

11: procedure SYNCHRONIZE( $W_{\text{local}}, t_{\text{local}}$ )
12:    $t_{\text{latest}} \leftarrow \text{GETLATESTREADY}()$ 
13:   if  $t_{\text{latest}} = t_{\text{local}}$  then                                 $\triangleright$  Already synchronized
14:     return  $W_{\text{local}}$ 
15:   end if
16:   if  $t_{\text{latest}} = t_{\text{local}} + 1$  then                                 $\triangleright$  Fast path
17:      $P, h \leftarrow \text{DOWNLOADDELTA}(t_{\text{latest}})$ 
18:      $W_{\text{new}} \leftarrow \text{DECODE}(W_{\text{local}}, P)$ 
19:     assert  $\text{SHA256}(W_{\text{new}}) = h$                                  $\triangleright$  Verify integrity
20:   else                                 $\triangleright$  Slow path: cold start or missed steps
21:      $t_{\text{anchor}} \leftarrow \lfloor t_{\text{latest}}/k \rfloor \cdot k$ 
22:      $W_{\text{new}} \leftarrow \text{DOWNLOADFULL}(t_{\text{anchor}})$ 
23:     for  $t' \leftarrow t_{\text{anchor}} + 1$  to  $t_{\text{latest}}$  do
24:        $P, h \leftarrow \text{DOWNLOADDELTA}(t')$ 
25:        $W_{\text{new}} \leftarrow \text{DECODE}(W_{\text{new}}, P)$ 
26:       assert  $\text{SHA256}(W_{\text{new}}) = h$                                  $\triangleright$  Verify integrity
27:     end for
28:   end if
29:   return  $W_{\text{new}}$ 
30: end procedure

```

---

**Ready markers.** The protocol uses explicit ready markers to ensure atomicity. A checkpoint is only considered available after all its constituent files have been uploaded. This prevents inference nodes from reading partially uploaded checkpoints.

**Concurrent uploads.** At anchor windows, both FULL and DELTA checkpoints are uploaded. The DELTA upload proceeds synchronously, while the FULL upload runs asynchronously in the background. This ensures that the delta chain remains uninterrupted even if the large FULL upload is slow.

## G.2 Anchor Interval Selection

The anchor interval  $k$  determines how often full checkpoints are published. The choice involves three trade-offs:

- **Cold-start latency:** New nodes must download one anchor plus up to  $k - 1$  deltas. For a 7B model, this is  $14 \text{ GB} + (k - 1) \times 108 \text{ MB}$ .
- **Storage:** Over  $n$  steps, storage is approximately  $\lceil n/k \rceil \times 14 \text{ GB} + n \times 108 \text{ MB}$ .
- **Trainer upload bandwidth:** Full checkpoints are  $\sim 130 \times$  larger than deltas, so lower  $k$  places significant upload burden on the trainer.

**Practical guidance.** In bandwidth-constrained scenarios (the primary use case for PULSE), higher  $k$  is generally preferable. Steady-state inference nodes use the fast path (single delta) regardless of  $k$ ,

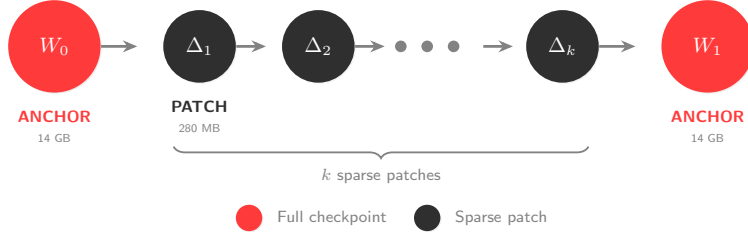


Figure 14: **Checkpoint chain structure.** Full checkpoints (anchors) are published every  $k$  steps; between anchors, only sparse patches are transmitted. This structure enables the fast path (single patch application) for steady-state nodes while providing recovery points for late joiners via the slow path (anchor download plus patch chain). See Algorithm 4 for the formal protocol.

so the anchor interval only affects cold starts and trainer uploads. We use  $k = 50$  in our experiments, balancing reasonable cold-start times ( $\sim 5$  minutes at 400 Mbit/s) with minimal trainer overhead.

### G.3 Integrity Verification

Checkpoints may be corrupted during transmission or by malicious storage providers. PULSE employs multi-level integrity verification.

**File-level integrity.** Each checkpoint includes a signed manifest containing SHA256 hashes for all files. The manifest is signed with the trainer’s cryptographic key, preventing tampering by storage providers.

**Weight-level integrity.** Each delta includes a SHA256 hash of the *resulting* weights after application:

$$h_t = \text{SHA256}(\text{CONCAT}(\{W_t[p] : p \in \text{params}\})) \quad (27)$$

This enables end-to-end verification: after applying a delta chain, the consumer verifies that the reconstructed weights match the expected hash. Hash mismatches trigger automatic fallback to the slow path (re-download from anchor).

**Deterministic hashing.** To ensure hash reproducibility across hardware, we use a deterministic serialization order and canonical byte representations. The hash is computed over raw BF16 bit patterns, ensuring bitwise consistency.

### G.4 Failure Recovery

**Delta upload failure.** If a delta upload fails, the system falls back to uploading a full checkpoint. This ensures the chain remains valid even under network instability.

**Hash verification failure.** If an inference node detects a hash mismatch, it discards the corrupted state and re-synchronizes from the nearest anchor. This self-healing behavior ensures eventual consistency.

**Network partitions.** Inference nodes operate independently and can tolerate arbitrary network partitions. Upon reconnection, they synchronize to the latest checkpoint using the slow path if necessary.

### G.5 End-to-End Latency Analysis

We measure end-to-end synchronization latency on commodity hardware with 400 Mb/s network bandwidth. Table 9 breaks down the latency for three scenarios.

Table 9: End-to-end latency breakdown for 7B model synchronization ( $400\text{ Mb/s}$  network). The slow path assumes recovery requiring 9 delta applications.

Operation	Fast Path	Slow Path	Cold Start
<i>Download</i>			
Full checkpoint (14 GB)	–	280 s	280 s
Delta(s) ( $\sim 108\text{ MB}$ each)	2.2 s	19.8 s	–
<i>Processing</i>			
Decompression (zstd)	0.6 s	5.4 s	–
Delta application	0.3 s	2.7 s	–
Hash verification	0.8 s	0.8 s	0.8 s
<b>Total</b>	<b>3.9 s</b>	<b>308.7 s</b>	<b>280.8 s</b>

**Fast path dominance.** In steady-state operation, inference nodes use the fast path exclusively, achieving synchronization in  $\sim 4\text{ s}$ . This represents over  $100\times$  speedup compared to downloading the full  $14\text{ GB}$  checkpoint.

**Parallelization.** Delta downloads and applications can be pipelined: while applying delta  $i$ , download delta  $i + 1$  in parallel. This reduces slow path latency by  $\sim 30\%$  in our implementation.

## G.6 Retention Policy

Without cleanup, storage grows linearly. PULSE implements an automatic retention policy.

**Delta retention.** Keep the most recent 100 delta checkpoints. Older deltas are deleted, but their anchors are preserved if any retained delta references them.

**Anchor retention.** Keep the most recent 10 full checkpoints, plus any anchors referenced by retained deltas.

**Storage bounds.** With default settings, maximum storage for a 7B model is:

$$S_{\max} = 10 \cdot 14\text{ GB} + 100 \cdot 108\text{ MB} \approx 151\text{ GB} \quad (28)$$